J. Fluid Mech. (2019), *vol.* 859, *pp.* 992–1021. © Cambridge University Press 2018
doi:10.1017/jfm.2018.812

Thermocapillary flows on heated substrates with sinusoidal topography

Jaehyun Yoo[1], **Jaewook Nam**[1,†] **and Kyung Hyun Ahn**[1]

[1]School of Chemical and Biological Engineering, Institute of Chemical Processes, Seoul National University, 1 Gwanak-ro, Gwanak-gu, Seoul 08826, Korea

(Received 4 February 2018; revised 2 October 2018; accepted 6 October 2018; first published online 27 November 2018)

Two-dimensional steady thermocapillary flows in a liquid layer over a substrate, which has a uniform temperature and sinusoidal topography, are investigated by asymptotic theory. Here, the buoyancy effect is negligible and the interface is not significantly disturbed under low Marangoni number and low capillary number. A temperature gradient along the gas/liquid interface causes recirculating flows. For a small aspect ratio, which yields a sinusoidal topography with a long wavelength relative to the mean depth of the liquid layer, the second-order solutions are obtained analytically. The basic solutions show vertical diffusion of heat and vorticity from the substrate and interface, respectively. In the second corrections, the horizontal diffusion of heat weakens the overall flow and the convection of heat intensifies it.

Key words: capillary flows, Marangoni convection

1. Introduction

An interaction between two different fluid molecules across an interface causes a surface tension. Since the surface tension is a state function, it depends on the temperature, composition, electric charge density, etc. of the fluids (Scriven 1960). Therefore, a temperature gradient along the interface invokes a surface-tension gradient, which makes static equilibrium impossible. These phenomena are called thermocapillary flows or thermal Marangoni flows.

Such flows are observed in several systems, including combustion processes (Sirignano & Glassman 1970; Torrance 1971), welding pools (Russo, Akau & Jellison 1990; Mills *et al.* 1998), crystal-growth processes (Schwabe & Scharmann 1981; Cuvelier & Driessen 1986), droplet coalescence and formation (Gupta *et al.* 2016; Geri *et al.* 2017), etc.

In this study, we focus on thermocapillary flows in liquid layers on heated substrates, which can be encountered in liquid film coatings (Weinstein & Palmer 1997). Usually, a flat substrate has been considered for exploring thermocapillary flows under a liquid layer (Birikh 1966; Münch 2002; Evans & Münch 2006). Thermal instabilities such as Bénard convection were observed (Eckert, Bestehorn & Thess 1998; Tomita & Abe 2000; Schatz & Neitzel 2001). Recently, however, non-flat or patterned substrates have been employed in liquid film coatings. In wearable

† Email address for correspondence: jaewooknam@snu.ac.kr

https://doi.org/10.1017/jfm.2018.812 Published online by Cambridge University Press

electronics, single fibres with electronic functions are converted into fabric structures to achieve flexibility or transparency (Zeng *et al.* 2014). Coating, levelling and drying processes are conducted over those substrates with patterns. Such electronics are used to monitor the physical activity and health status in the applications of outdoor clothing or medical devices. Owing to these practical interests, several experimental and numerical studies were carried out for geometrically-patterned substrates (Ismagilov *et al.* 2001; Alexeev, Gambaryan-Roisman & Stephan 2005; Fath *et al.* 2015). A lubrication-theory-based model is typically used for describing hydrodynamics and energy transport to determine the evolution of the multicomponent thin films (Saprykin *et al.* 2007; Frumkin & Oron 2016; Pham, Cheng & Kumar 2017).

The asymptotic theory has been successfully used to analytically study numerous types of convection due to buoyancy or thermocapillary force. Cormack, Leal & Imberger (1974) considered buoyancy-driven flows in a rectangular container bounded by differently heated lateral walls and Poulikakos & Bejan (1983) treated flows in an attic space heated from below. Sen & Davis (1982) and Strani, Piva & Graziani (1983) studied thermocapillary flows in a rectangular slot bounded by differently heated lateral walls.

Apart from those successful studies, a liquid layer over a patterned substrate has rarely been treated by the asymptotic theory. Gambaryan-Roisman, Alexeev & Stephan (2005), Kabova *et al.* (2006) and Gambaryan-Roisman & Stephan (2007) obtained the first-order solutions over patterned substrates in the limit of a long wavelength of the pattern, with a shallow amplitude or a small capillary number, whereas Sadiq (2012) and Sadiq, Gambaryan-Roisman & Stephan (2012) used the integral boundary method on the longitudinal grooves.

In this study, we explore flow conditions different from the previous studies that result in different approximated solutions. Moreover, most of the previous studies focused on the shape of the interface and investigated the stability of flows by using the long-wave film evolution equation. They examined gas/liquid interface perturbations to describe the rupture and local thinning behaviour of thin liquid films. In contrast, we choose the conditions free from flow instability and systematically reveal how the temperature and flow fields change depending on system parameters including substrate topography.

Here, we consider two-dimensional steady thermocapillary flows in a horizontally unbounded liquid layer over a substrate with sinusoidal topography, where the substrate has a uniform temperature that is higher than that of the gas/liquid interface. The thickness of the layer between the interface and the substrate varies along the horizontal direction because of the substrate topography. This thickness variation induces an interfacial temperature gradient that leads to the flows. The second-order solutions can be obtained analytically for a small aspect ratio, which yields a long wavelength of the sinusoidal topography relative to the mean depth of the coated liquid layer.

In the present work, the liquid layer between the interface and the substrate is sufficiently thin so that the buoyancy force due to the density gradient inside the layer is negligible. Instead, recirculating flows are due to the thermocapillary force along the interface. The liquid layer is, however, relatively thick in order to not allow interactions between the interface and the substrate, such as disjoining pressure (Teletzke, Davis & Scriven 1988). Furthermore, the Marangoni number is low, such that the resulting weak flows do not significantly disturb the interface, which is supported by low capillary number. Therefore, the disturbance of the interface

https://doi.org/10.1017/jfm.2018.812 Published online by Cambridge University Press

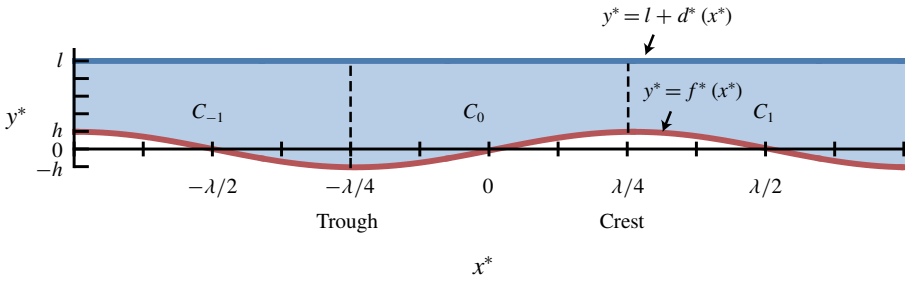


FIGURE 1. (Colour online) Flow domain over the substrate with sinusoidal topography. C_n represents the nth unit cell and the dashed vertical lines are the boundaries between the unit cells. See text for the x^* range defined for each cell.

shape vanishes in the second-order solutions, which greatly simplifies the analysis. Subsequently, we provide details of the magnitudes of key dimensionless numbers associated with the flow conditions discussed above.

We use the standard method of asymptotic analysis to consider the problem described above. The geometry, parameters and equations that govern the system are defined in § 2. The asymptotic solutions from energy and momentum conservation are represented and discussed in § 3, and § 4 presents the validation of the asymptotic solutions by comparing them with numerical solutions.

2. Mathematical descriptions

The liquid layer is coated over the substrate and aligned in the x^* direction. The sinusoidal function describing the shape of the substrate is

$$f^*(x^*) = h \sin \frac{2\pi}{\lambda} x^*, \tag{2.1}$$

where h is the amplitude and λ is the wavelength. Therefore, the substrate has troughs located at $x^* = n\lambda - \lambda/4$ and crests at $x^* = n\lambda + \lambda/4$, where n is an arbitrary integer. The vertical location of the interface is $y^* = l + d^*(x^*)$. The mean layer depth, when the interface is flat, is defined by l, and $d^*(x^*)$ is the disturbance from the flat interface.

The flow domain is horizontally unbounded, and it has symmetry and periodicity in the horizontal direction over the substrate with sinusoidal topography. One can define a unit cell region C_n bounded by $x^* = n\lambda/2 - \lambda/4$ and $x^* = n\lambda/2 + \lambda/4$ as a primary repeating building block of the flow domain. Adjacent C_n and C_{n+1} are symmetric across the vertical boundaries located at troughs or crests of the substrate, and C_n and C_{n+2} are periodic in every other cell. An example of the unit cells C_{-1}, C_0, and C_1 is depicted in figure 1.

A is defined as the aspect ratio of C_n multiplied by π:

$$A = \pi \frac{l}{\lambda/2}, \tag{2.2}$$

and the ratio of the amplitude of the substrate topography to the mean depth of the liquid is

$$H = \frac{h}{l}. \tag{2.3}$$

https://doi.org/10.1017/jfm.2018.812 Published online by Cambridge University Press

Two-dimensional steady flows in the absence of gravity are governed by energy, momentum and mass conservation equations (Sen & Davis 1982; Strani *et al.* 1983):

$$u^*\frac{\partial T^*}{\partial x^*}+v^*\frac{\partial T^*}{\partial y^*}=\kappa\nabla^{*2}T^*, \tag{2.4}$$

$$u^*\frac{\partial u^*}{\partial x^*}+v^*\frac{\partial u^*}{\partial y^*}=-\frac{1}{\rho}\frac{\partial p^*}{\partial x^*}+\nu\nabla^{*2}u^*, \tag{2.5}$$

$$u^*\frac{\partial v^*}{\partial x^*}+v^*\frac{\partial v^*}{\partial y^*}=-\frac{1}{\rho}\frac{\partial p^*}{\partial y^*}+\nu\nabla^{*2}v^*, \tag{2.6}$$

$$\frac{\partial u^*}{\partial x^*}+\frac{\partial v^*}{\partial y^*}=0, \tag{2.7}$$

where p^*, T^*, u^* and v^* are the pressure, temperature and horizontal and vertical velocity components, respectively. κ, ρ and ν are the thermal diffusivity, liquid density and kinematic viscosity, respectively, at the reference temperature T^{r*} of the liquid. Introducing the stream function ψ^* defined by

$$u^*=\frac{\partial\psi^*}{\partial y^*},\quad v^*=-\frac{\partial\psi^*}{\partial x^*}, \tag{2.8a,b}$$

one can reduce (2.5), (2.6) and (2.7) to

$$\frac{\partial\psi^*}{\partial y^*}\frac{\partial\omega^*}{\partial x^*}-\frac{\partial\psi^*}{\partial x^*}\frac{\partial\omega^*}{\partial y^*}=\nu\nabla^{*2}\omega^*, \tag{2.9}$$

$$\omega^*=-\frac{\partial^2\psi^*}{\partial x^{*2}}-\frac{\partial^2\psi^*}{\partial y^{*2}}, \tag{2.10}$$

where ω^* is the vorticity.

The liquid layer is heated from below by the substrate of uniform temperature T^{s*} and is cooled by a gas of the bulk temperature T^{g*} above the layer. Here, we shall use the linear equation of state for surface tension with respect to temperature:

$$\sigma(T^*)=\sigma_0-\gamma(T^*-T^{i*}), \tag{2.11}$$

where $\gamma=-\mathrm{d}\sigma/\mathrm{d}T^*>0$ and σ_0 is the surface tension at a characteristic temperature at the interface T^{i*} (Sen & Davis 1982). The liquid layer satisfies a no-slip condition at the substrate and a stress jump at the gas/liquid interface in the normal and the tangential directions. Therefore, the corresponding vertical boundary conditions for (2.4) and (2.9) are

$$-\boldsymbol{n}\cdot\boldsymbol{\nabla}^*(k_lT^*)=h_i(T^*-T^{g*}),\quad \text{on } y^*=l+d^*(x^*), \tag{2.12}$$

$$T^*=T^{s*},\quad \text{on } y^*=f^*(x^*), \tag{2.13}$$

$$\left.\begin{aligned}\boldsymbol{nn}:\boldsymbol{S}^*&=\sigma K^*,\\ \boldsymbol{nt}:\boldsymbol{S}^*&=-\gamma(\boldsymbol{t}\cdot\boldsymbol{\nabla}^*T^*),\\ v^*&=u^*\frac{\partial d^*}{\partial x^*},\end{aligned}\right\}\quad \text{on } y^*=l+d^*(x^*), \tag{2.14}$$

$$\psi^*=\frac{\partial\psi^*}{\partial y^*}=0,\quad \text{on } y^*=f^*(x^*), \tag{2.15}$$

https://doi.org/10.1017/jfm.2018.812 Published online by Cambridge University Press

where $\boldsymbol{S}^* = -p^*\boldsymbol{I} + 2\mu\boldsymbol{D}^*$ is the stress tensor of the liquid; the strain rate tensor $\boldsymbol{D}^*$ is defined by

$$\boldsymbol{D}^* = \begin{bmatrix} \dfrac{\partial u^*}{\partial x^*} & \dfrac{1}{2}\left(\dfrac{\partial u^*}{\partial y^*} + \dfrac{\partial v^*}{\partial x^*}\right) \\ \dfrac{1}{2}\left(\dfrac{\partial u^*}{\partial y^*} + \dfrac{\partial v^*}{\partial x^*}\right) & \dfrac{\partial v^*}{\partial y^*} \end{bmatrix}. \tag{2.16}$$

μ, k_l and h_i are the dynamic viscosity of the liquid, heat conductivity of the liquid and heat transfer coefficient of the gas side near the interface, respectively, all referred to T^{r*}. The unit outward normal vector $\boldsymbol{n}$, unit tangent vector $\boldsymbol{t}$ and curvature K^* of the interface are given by

$$\boldsymbol{n} = \frac{1}{N}\begin{pmatrix} -\dfrac{\partial d^*}{\partial x^*} & 1 \end{pmatrix}, \quad \boldsymbol{t} = \frac{1}{N}\begin{pmatrix} 1 & \dfrac{\partial d^*}{\partial x^*} \end{pmatrix}, \quad K^* = \frac{1}{N^3}\frac{\partial^2 d^*}{\partial x^{*2}}, \tag{2.17a–c}$$

where $N = [1 + (\partial d^*/\partial x^*)^2]^{1/2}$. Note that there is no horizontal boundary. Therefore, the temperature and flow fields inherit the symmetry and periodicity of the flow domain.

Apart from the above boundary conditions, the mass is conserved at any x^*, which leads to the condition of no net mass flow (Sen & Davis 1982):

$$\int_{f^*(x^*)}^{l+d^*(x^*)} u^*\,\mathrm{d}y^* = 0. \tag{2.18}$$

This produces the additional boundary condition for the stream function

$$\psi^* = 0, \quad \text{on } y^* = l + d^*(x^*). \tag{2.19}$$

The characteristic temperature T^{i*} and temperature difference ΔT^{i*} at the interface are defined under the assumption of purely vertical heat diffusion inside the liquid layer and the flat interface. Since f^* is small compared to l, the continuity of the heat fluxes inside of and at the surface of the liquid layer approximately satisfies the following relation,

$$k_l\frac{T^{s*} - T^*|_{y^*=l}}{l - f^*} \approx h_i(T^{i*} - T^{g*}). \tag{2.20}$$

For $T^*|_{y^*=l}$, rearranging (2.20),

$$T^*|_{y^*=l} \approx T^{s*} - Bi\left(1 - \frac{f^*}{l}\right)(T^{i*} - T^{g*}). \tag{2.21}$$

$Bi = h_i l/k_l$ is the Biot number that represents the ratio of the heat transfer resistances inside of and at the surface of a liquid layer. T^{i*} and ΔT^{i*} are defined as the temperature at the interface with $f^* = 0$ and the temperature difference between T^{it*} and T^{ic*}, respectively. Herein, T^{it*} and T^{ic*} are the temperatures at the interface above the trough ($f^* = -h$) and crest ($f^* = h$), respectively, of the substrate. Using (2.21), the characteristic variables are defined as

$$T^{i*} = \frac{T^{s*} + Bi\,T^{g*}}{1 + Bi}, \tag{2.22}$$

$$\Delta T^{i*} = 2H(T^{s*} - T^{i*}). \tag{2.23}$$

https://doi.org/10.1017/jfm.2018.812 Published online by Cambridge University Press

Here, we scale the system by introducing the following quantities:

$$x=\frac{x^*}{\lambda/2\pi},\quad y=\frac{y^*}{l},\quad u=\frac{u^*}{U},\quad v=\frac{v^*}{AU},\quad p=\frac{p^*}{\mu U\lambda/2\pi l^2},\quad T=\frac{T^*-T^{i*}}{\Delta T^{i*}}. \tag{2.24a–f}$$

Using these variables, the characteristic velocity of the system U can be derived from the balance between the jump in shear stress along the interface and the surface-tension gradient (Sen & Davis 1982):

$$U=\frac{\gamma\Delta T^{i*}}{\mu}A. \tag{2.25}$$

Using the above scaling, the function describing the substrate becomes

$$f(x)=H\hat{f}(x)=H\sin x, \tag{2.26}$$

where the dimensionless wavelength and amplitude are 2π and H, respectively. Therefore, C_n is bounded by $x=n\pi-\pi/2$ and $x=n\pi+\pi/2$. The normalised substrate shape is defined by $\hat{f}(x)=\sin x$. In this study, we consider $H=O(0.1)$. The geometry of the liquid layer is defined by A and H.

The dimensionless governing equations can be written as follows:

$$MaA(\psi_yT_x-\psi_xT_y)=A^2T_{xx}+T_{yy}, \tag{2.27}$$

$$ReA(\psi_y\omega_x-\psi_x\omega_y)=A^2\omega_{xx}+\omega_{yy}, \tag{2.28}$$

$$\omega=-A^2\psi_{xx}-\psi_{yy}. \tag{2.29}$$

The Marangoni number Ma, Reynolds number Re, Prandtl number Pr and capillary number Ca are defined by

$$Ma=\frac{Ul}{\kappa},\quad Re=\frac{Ul}{\nu},\quad Pr=\frac{\nu}{\kappa},\quad Ca=\frac{\mu U}{\sigma_0} \tag{2.30a–d}$$

and $Re=Ma/Pr$. The boundary conditions (2.12)–(2.15) transform to

$$\frac{T_y-A^2d_xT_x}{(1+A^2d_x^2)^{1/2}}=-Bi\,T-\frac{1}{2H},\quad \text{on } y=1+d(x), \tag{2.31}$$

$$T=\frac{1}{2H},\quad \text{on } y=f(x), \tag{2.32}$$

$$\left.\begin{aligned}-p+\frac{2A^2}{(1+A^2d_x^2)}[(v_y-d_xu_y)+A^2d_x(-v_x+d_xu_x)]\\ =\frac{A^2d_{xx}}{(1+A^2d_x^2)^{3/2}}\left(\frac{A}{Ca}-T\right),\\ (u_y+A^2v_x)(1-A^2d_x^2)+2A^2d_x(v_y-u_x)\\ =-(1+A^2d_x^2)^{1/2}(T_x+d_xT_y),\\ v=ud_x,\end{aligned}\right\}\quad \text{on } y=1+d(x), \tag{2.33}$$

$$\psi=\psi_y=0,\quad \text{on } y=f(x), \tag{2.34}$$

and the condition of no net mass flow (2.19) becomes

$$\psi=0,\quad \text{on } y=1+d(x). \tag{2.35}$$

https://doi.org/10.1017/jfm.2018.812 Published online by Cambridge University Press

3. Asymptotic solutions

The liquid layer system considered in this study has a small A, i.e. $A \ll 1$. In particular, we treat the system in the asymptotic limit as $A \to 0$. In this limit, the complete temperature and flow fields may be determined by a regular perturbation of (2.27)–(2.29) and (2.31)–(2.35) in a small perturbation quantity A. The solutions can be described by asymptotic expansions with the asymptotic sequence $\{A^m\}$, where m is an integer, as $A \to 0$:

$$\left.\begin{aligned} T(x,y) &= T_0(x,y) + AT_1(x,y) + A^2T_2(x,y) + \cdots, \\ \omega(x,y) &= \omega_0(x,y) + A\omega_1(x,y) + A^2\omega_2(x,y) + \cdots, \\ \psi(x,y) &= \psi_0(x,y) + A\psi_1(x,y) + A^2\psi_2(x,y) + \cdots, \\ p(x,y) &= p_0(x,y) + Ap_1(x,y) + A^2p_2(x,y) + \cdots, \\ d(x) &= Ad_1(x) + A^2d_2(x) + \cdots, \end{aligned}\right\} \tag{3.1}$$

and $u(x,y)$ and $v(x,y)$ can be derived from (2.8). Using the expansions, the solutions of the governing equations can be obtained by a systematic scheme of successive approximations (Van Dyke 1964). In the present work, the second-order solutions are investigated. They are sufficient to describe the temperature and flow fields when compared with the numerical solutions described in § 4. We obtain the solutions applicable over the entire liquid layer, but the solutions are depicted in C_0 only.

In this study, the analysis is based on the following asymptotic limits of the dimensionless parameters:

$$Ma = \overline{Ma}\,A, \quad Re = \overline{Re}\,A, \quad Ca = \overline{Ca}\,A^6, \tag{3.2a–c}$$

with $\overline{Ma}$, $\overline{Re}$ and $\overline{Ca}$ of $O(1)$. The order of A in Ma and Re, which implies $Pr = O(1)$, corresponds to mild heating and slow liquid convections. The convection terms appear from the second corrections onward.

Given equation (2.25), the capillary number used here can be interpreted as a crispation number relating the effect of the surface-tension gradient to that of the surface tension, and $Ca = O(A^6)$ implies that a high surface tension stabilises a flat interface in this system. For organic liquids used in liquid film coatings, Ca has the order of $10^{-2}\Delta T^{i*}A$ based on the material properties in Kőrösi & Kováts (1981), Poling *et al.* (2008). Therefore, the proposed model is physically relevant when the order of ΔT^{i*} becomes $10^2A^5\,^\circ$C, for satisfying $Ca = O(A^6)$. For example, using a toluene solution based on the material properties of toluene in Kőrösi & Kováts (1981) with $l = 0.1$ mm, $\lambda/2\pi = 0.5$ mm, and hence $A = 0.2$, the system is required to have $\Delta T^{i*} \approx 0.1\,^\circ$C.

Considering the order of Ca, the jump in the normal stress from (2.33) leads to

$$d_1 = 0, \quad d_2 = 0, \tag{3.3a,b}$$

and the first non-trivial correction appears at $O(A^3)$. In the second-order solutions, the disturbance of the interface shape vanishes, and therefore, the position of the interface is fixed, which proves that the flat interface is relevant. In addition, the steady-state solutions in this study are stable due to the order of Ca when applying a usual procedure for linear stability analysis in Oron, Davis & Bankoff (1997) and Pham *et al.* (2017).

From the normal stress condition, the third and higher corrections for the interface shape can be calculated, such as $d_{3,xx}(x) = -p_0$ in the leading order. As only the

https://doi.org/10.1017/jfm.2018.812 Published online by Cambridge University Press

second-order solutions are considered in this study, the normal stress condition need not be treated. Using (3.3), the kinematic condition in (2.33) leads to

$$v_0 = 0, \quad v_1 = 0, \quad v_2 = 0, \quad \text{on } y = 1, \tag{3.4a–c}$$

which is compatible with the condition of no net mass flow (2.35). Thus, only the jump in the tangential stress needs to be considered for the second-order solutions. Bi is chosen as $O(1)$, as used in other studies (Sen & Davis 1982; Eckert *et al.* 1998).

3.1. *Basic solutions*

Substituting the expansions (3.1) into (2.27)–(2.29) and (2.31)–(2.35), we find the leading-order equations

$$T_{0,yy} = 0, \tag{3.5}$$
$$\omega_{0,yy} = 0, \tag{3.6}$$
$$\omega_0 = -\psi_{0,yy}, \tag{3.7}$$

with the boundary conditions

$$T_{0,y} = -Bi\, T_0 - \frac{1}{2H}, \quad \text{on } y = 1, \tag{3.8}$$
$$T_0 = \frac{1}{2H}, \quad \text{on } y = f(x), \tag{3.9}$$
$$\omega_0 = T_{0,x}, \quad \text{on } y = 1, \tag{3.10}$$
$$\psi_0 = \psi_{0,y} = 0, \quad \text{on } y = f(x), \tag{3.11}$$

where the interfacial vorticity is defined by $\omega_0|_{y=1} = -u_{0,y}|_{y=1}$ in (3.10), and the condition of no net mass flow

$$\psi_0 = 0, \quad \text{on } y = 1. \tag{3.12}$$

The governing equations (3.5) and (3.6) show that the vertical diffusion is the only transport mechanism of heat and vorticity for the basic solutions. Equations (3.9) and (3.10) indicate that the heat and vorticity arise from the substrate and the interface, respectively.

The solution for T_0 that satisfies (3.5), (3.8) and (3.9) is

$$T_0(x, y) = \phi_0(x)\, \bar{T}_0(y) - \frac{1}{2Bi\, H}, \tag{3.13}$$

where

$$\bar{T}_0(y) = -y + 1 + \frac{1}{Bi}, \tag{3.14}$$

and

$$\phi_0(x) = \frac{1 + Bi}{2H(1 + Bi - Bi f(x))}. \tag{3.15}$$

In this study, we approximate the results from asymptotic solutions for a small magnitude $H = O(0.1)$ in order to interpret the effects of substrate topography and the heat-transfer characteristics on the temperature and flow fields. The approximation

https://doi.org/10.1017/jfm.2018.812 Published online by Cambridge University Press

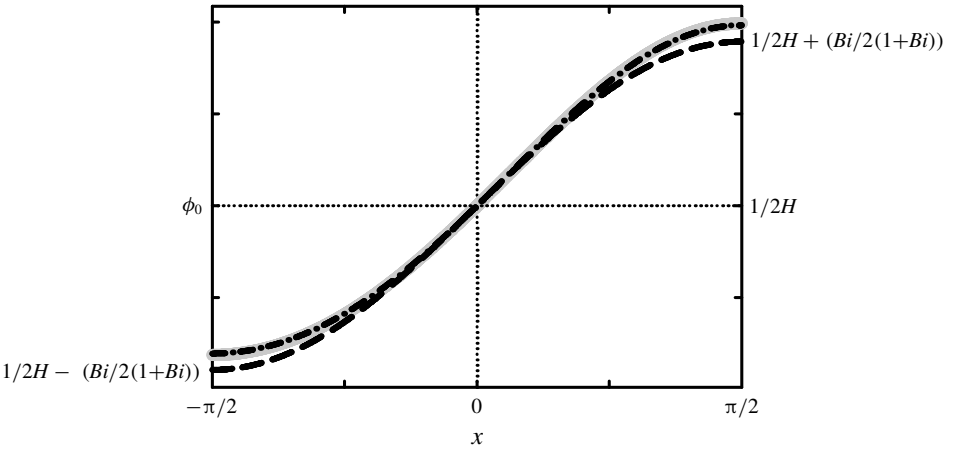


FIGURE 2. Heat flux $\phi_0(x)$ for $Bi = 1$ and $H = 0.2$: —— (grey), exact one in (3.15); – – –, zeroth order approximation in H from (3.16); – · – · –, linear approximation in H in (3.16).

is based on Taylor series expansions with respect to H around $H = 0$. For $\phi_0(x)$, the expression $H\phi_0(x)$ is approximated, and the terms up to the order of H are retained:

$$\phi_0(x) \approx \frac{1}{2H} + \frac{Bi}{2(1+Bi)}\hat{f}(x) + \frac{Bi^2}{2(1+Bi)^2}\hat{f}^2(x)H. \tag{3.16}$$

According to figure 2, this linear approximation is reasonable for this study.

The vertical heat diffusion causes T_0 to linearly depend on y, as shown in $\bar{T}_0(y)$. Meanwhile, the dependence of T_0 on x is isolated in $\phi_0(x)$, which is essentially the dimensionless heat flux, $-T_{0,y}$. $f(x)$ causes $\phi_0(x)$ to increase along x in C_0, as indicated by (3.15). The first term in (3.16) is the base value and the second term shows that the flux depends on $\hat{f}(x)$, and the amplitude of the second term is $(1/2)Bi(1 + Bi)^{-1}$. According to figure 2, $\phi_0(x)$ can be adequately described by using the zeroth approximation in H. Therefore, $\phi_0(x)$ mainly reflects the effect of the normalised substrate shape and the ratio of the internal to external heat transfer resistance of the liquid layer on T_0. The remaining linear contribution in H affects $\phi_0(x)$ slightly. Consequently, $\bar{T}_0(y)$ controls the temperature vertically, and $\phi_0(x)$ does so horizontally, as shown in the temperature field for the basic solution depicted in figure 3(*a*).

As we discussed, the chief cause of flows is the thermocapillary force, which is generated by the non-uniform interfacial temperature. The interfacial temperature is

$$T_0(x, 1) = \frac{f(x)}{2H(1 + Bi - Bif(x))} \tag{3.17a}$$

$$\approx \frac{1}{2(1+Bi)}\hat{f}(x) + \frac{Bi}{2(1+Bi)^2}\hat{f}^2(x)H. \tag{3.17b}$$

As expected, $f(x)$ causes $T_0(x, 1)$ to increase along x in C_0, as shown in (3.17*a*). Figure 3(*b*) shows that the $T_0(x, 1)$ profile can be adequately described by using the zeroth approximation in H. The first term in equation (3.17*b*) shows that the normalised substrate shape mainly governs the interfacial T_0 profile with its amplitude $(1/2)(1 + Bi)^{-1}$. The remaining linear contribution in H slightly affects the $T_0(x, 1)$ profile.

https://doi.org/10.1017/jfm.2018.812 Published online by Cambridge University Press

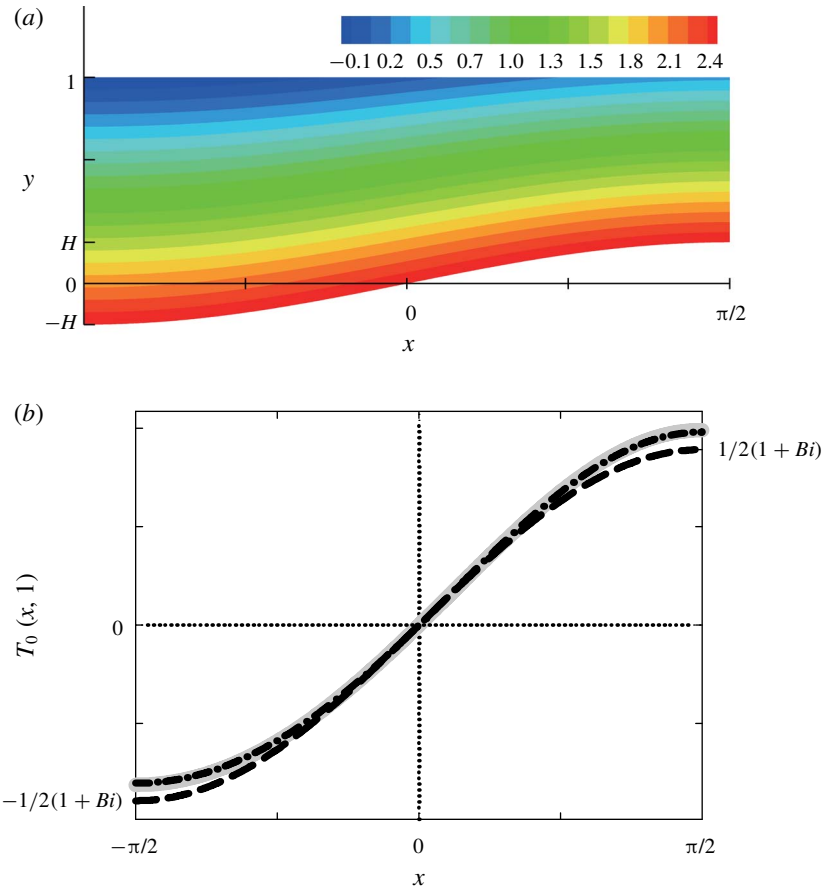


FIGURE 3. (Colour online) (*a*) Contour plot of T_0, and (*b*) $T_0(x, 1)$ profile corresponding to x: —— (grey), exact one in (3.17*a*); – – –, zeroth order approximation in H from (3.17*b*); – · – · –, linear approximation in H in (3.17*b*). $Bi = 1$ and $H = 0.2$ for all plots.

The interfacial temperature gradient, $T_{0,x}|_{y=1}$, is

$$\Theta_0^i(x) = \frac{1+Bi}{2H(1+Bi-Bif(x))^2} f'(x) \tag{3.18a}$$

$$\approx \frac{1}{2(1+Bi)} \hat{f}'(x) + \frac{Bi}{(1+Bi)^2} \hat{f}(x)\hat{f}'(x)H. \tag{3.18b}$$

$f(x)$ in $T_0(x, 1)$ causes the dependence of $\Theta_0^i(x)$ on $f'(x)$, which induces $\Theta_0^i(x)$ to be always positive in C_0, as shown in (3.18*a*). Figure 4 shows that the linear approximation in (3.18*b*) is reasonable. The first term in (3.18*b*) explicitly shows that $\Theta_0^i(x)$ depends on $\hat{f}'(x)$, in this study $\cos x$, which is the normalised substrate slope, and the amplitude of the first term is $(1/2)(1 + Bi)^{-1}$. According to figure 4, the profile of $\Theta_0^i(x)$ can be roughly captured by the zeroth approximation in H. Therefore, $\Theta_0^i(x)$ is mainly governed by the normalised substrate slope and the ratio of the internal to external heat transfer resistance of the liquid layer. The remaining

https://doi.org/10.1017/jfm.2018.812 Published online by Cambridge University Press

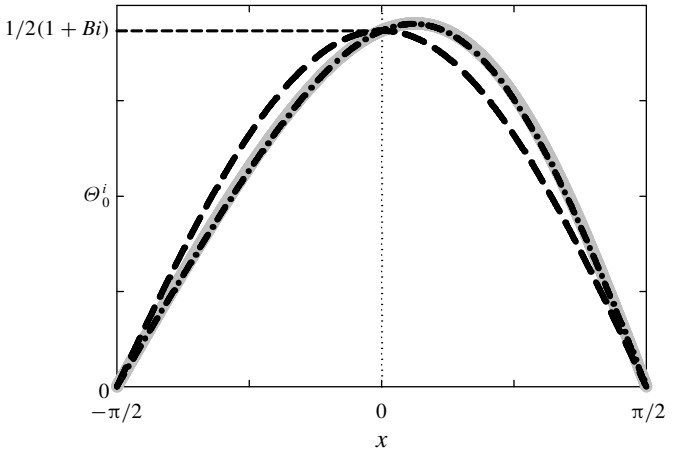


FIGURE 4. Interfacial temperature gradient $\Theta_0^i(x)$ for $Bi = 1$ and $H = 0.2$: —— (grey), exact one in (3.18*a*); – – –, zeroth order approximation in H from (3.18*b*); – · – · –, linear approximation in H in (3.18*b*).

linear contribution in H completes $\Theta_0^i(x)$ by marginally disrupting the symmetry across $x = 0$.

According to the boundary condition (3.10), the interfacial vorticity is generated by $\Theta_0^i(x)$. The vorticity propagates via the viscous diffusion, as governed by (3.6), which induces the flows in the leading order. Therefore, $\Theta_0^i(x)$ works as the driving force for the flows. As a result, a vortex appears inside the unit cell because flows cannot penetrate the boundaries of the cell, which will be established in this paper.

The solutions for ω_0, u_0 and ψ_0 can be obtained by solving (3.6), (3.7) and (3.10)–(3.12). They are

$$\omega_0(x, Y) = \Theta_0^i(x)\,\bar{\omega}_0(Y), \tag{3.19}$$

$$u_0(x, Y) = \Theta_0^i(x) D(x)\,\bar{u}_0(Y), \tag{3.20}$$

$$\psi_0(x, Y) = \Theta_0^i(x) D^2(x)\,\bar{\psi}_0(Y), \tag{3.21}$$

where $D(x) = 1 - f(x)$ is the depth of the liquid layer and $Y = (y - f(x))/D(x)$ is the vertical position rescaled by the depth. Here, we factored out $\Theta_0^i(x)$ or $D(x)$ from ω_0, u_0 and ψ_0 because, in x and Y coordinates, the effects of the substrate topography lie in $\Theta_0^i(x)$ and $D(x)$. Then, the remaining terms become

$$\bar{\omega}_0(Y) = \tfrac{3}{2}\left(Y - \tfrac{1}{3}\right), \tag{3.22}$$

$$\bar{u}_0(Y) = -\tfrac{3}{4}\left(Y - \tfrac{2}{3}\right) Y, \tag{3.23}$$

$$\bar{\psi}_0(Y) = -\tfrac{1}{4}(Y - 1)Y^2. \tag{3.24}$$

The vertical vorticity diffusion causes ω_0 to linearly depend on Y , as shown in $\bar{\omega}_0(Y)$. Similarly, the dependence of u and ψ on Y appears in $\bar{u}_0(Y)$ and $\bar{\psi}_0(Y)$, respectively.

Equation (3.19) can explain the vertical and horizontal changes in ω_0 shown in figure 5(*a*). $\bar{\omega}_0(Y)$ vertically controls the vorticity, and $\Theta_0^i(x)$ does so horizontally. Figure 5(*d*) shows that $\bar{\omega}_0$ is positive at the interface, decreases linearly as Y decreases, and changes sign at $Y = 1/3$. Because of the no-slip boundary condition, $\bar{\omega}_0$ becomes

https://doi.org/10.1017/jfm.2018.812 Published online by Cambridge University Press

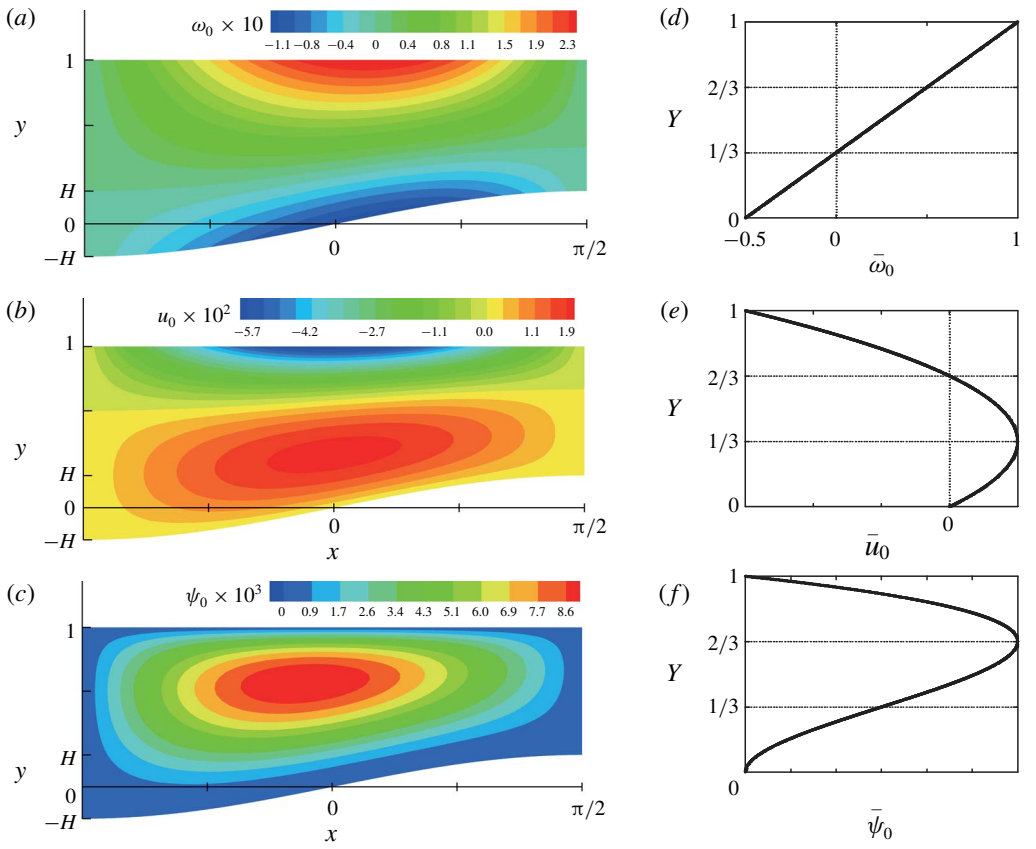


FIGURE 5. (Colour online) Contour plots of (*a*) ω_0, (*b*) u_0 and (*c*) ψ_0 for $Bi = 1$ and $H = 0.2$, and the plots of (*d*) $\bar{\omega}_0(Y)$, (*e*) $\bar{u}_0(Y)$ and (*f*) $\bar{\psi}_0(Y)$.

negative near the substrate. As indicated by $\Theta_0^i(x)$, figure 4 implies that the interfacial ω_0 has the maximum value near the centre and vanishes at both corners of the interface. Because of the symmetry between neighbouring unit cells, the sign of the vorticity changes across the cell boundaries.

This vorticity profile leads to a typical reversal flow inside the layer, as shown in figure 5(*b*). The horizontal velocity changes quadratically along Y and has a maximum magnitude at $Y = 1/3$, as plotted in figure 5(*e*). Note that the flow reversal occurs at $Y = 2/3$. Therefore, the vortex centre, which is characterised by vanishing velocity components, should exist at $Y = 2/3$ (Nam, Scriven & Carvalho 2009). The symmetric substrate topography causes the change in the sign of $\Theta_0^i(x)$ and the corresponding change in the direction of the horizontal velocity across the unit cell boundaries.

This reversal flow in the unit cell implies a circular streamline pattern, as shown in figure 5(*c*). The stream function changes cubically along Y and has the maximum value at $Y = 2/3$ and an inflexion point at $Y = 1/3$, as plotted in figure 5(*f*). The stream function vanishes at the unit cell boundaries because of the absence of the driving force, i.e. $\Theta_0^i = 0$. Owing to the no-penetration conditions, the stream function also vanishes on the substrate and the interface. Because the unit cell is surrounded by $\psi_0 = 0$, the flows cannot penetrate the boundaries of the cell. Note that all the stream function values on C_0 are positive because $\bar{\psi}_0(Y) > 0$ and $\Theta_0^i(x) > 0$. Therefore,

https://doi.org/10.1017/jfm.2018.812 Published online by Cambridge University Press

the recirculation direction is anticlockwise. However, the neighbouring cells, C_{-1} and C_1, have the opposite recirculation direction, which is due to $\Theta_0^i(x) < 0$. The inherent symmetry and periodicity of the solutions permit a straightforward reconstruction of the complete temperature and flow fields in the infinitely long liquid layer.

To summarise, the behaviours of the basic solutions along the vertical direction can be adequately represented by variables with the bar symbol, e.g. $\bar{T}_0(y)$ and $\bar{\omega}_0(Y)$. In this study, the heat flux $\phi_0(x)$ and the interfacial temperature gradient $\Theta_0^i(x)$ clearly show the effect of the substrate shape and slope, respectively, in combination with the ratio of the internal to external heat transfer resistance of the liquid layer on the basic solutions.

3.2. *First and second corrections*

To the first corrections, T_1, ω_1 and ψ_1 satisfy the set of equations

$$T_{1,yy} = 0, \tag{3.25}$$

$$\omega_{1,yy} = 0, \tag{3.26}$$

$$\omega_1 = -\psi_{1,yy}, \tag{3.27}$$

together with the boundary conditions

$$T_{1,y} = -Bi\, T_1, \quad \text{on } y = 1, \tag{3.28}$$

$$T_1 = 0, \quad \text{on } y = f(x), \tag{3.29}$$

$$\omega_1 = T_{1,x}, \quad \text{on } y = 1, \tag{3.30}$$

$$\psi_1 = \psi_{1,y} = 0, \quad \text{on } y = f(x), \tag{3.31}$$

where $\omega_1|_{y=1} = -u_{1,y}|_{y=1}$ in (3.30), and the condition of no net mass flow

$$\psi_1 = 0, \quad \text{on } y = 1. \tag{3.32}$$

Because the substrate no longer provides heat to change T_1, as indicated by the boundary condition (3.29), equations (3.25)–(3.27) have trivial solutions. Therefore, there are no first corrections, and only the second corrections are discussed in this section.

3.2.1. *Temperature field*

To the second correction, T_2 satisfies the governing equation

$$T_{2,yy} = -T_{0,xx} + \underbrace{\overline{Ma}(\psi_{0,y}T_{0,x} - \psi_{0,x}T_{0,y})}_{=q_2(x,y)}, \tag{3.33}$$

together with the boundary conditions

$$T_{2,y} = -Bi\, T_2, \quad \text{on } y = 1, \tag{3.34}$$

$$T_2 = 0, \quad \text{on } y = f(x). \tag{3.35}$$

$-T_{0,xx}$ is the term derived from the horizontal diffusion of T_0, and q_2 is the term derived from the convection of T_0 under the flows in the leading order.

T_2 is transported by a vertical diffusion similar to T_0, as described by (3.33). Unlike the leading order, however, T_2 is not generated from the substrate, but from the source terms $-T_{0,xx}$ and q_2. T_2 is the linear combination of two parts: $T_2 = T_2^D + T_2^C$, where superscripts D and C denote that the corresponding quantities arise from $-T_{0,xx}$ and q_2, respectively.

https://doi.org/10.1017/jfm.2018.812 Published online by Cambridge University Press

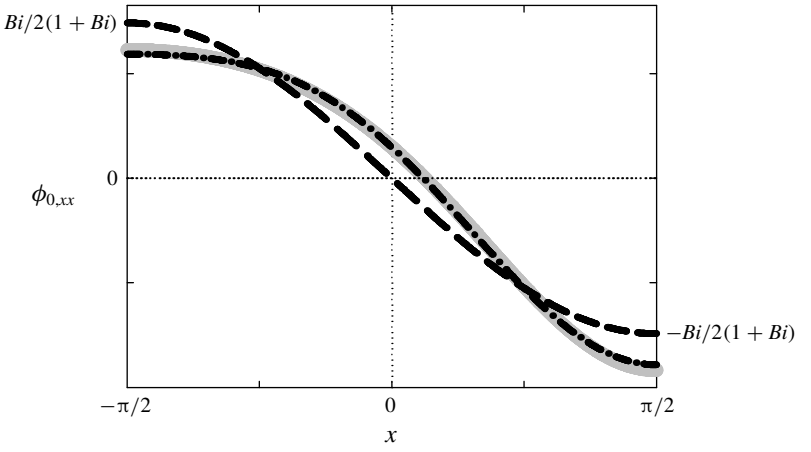


FIGURE 6. $\phi_{0,xx}(x)$ for $Bi=1$ and $H=0.2$: —— (grey), exact one in (3.38*a*); – – –, zeroth order approximation in H from (3.38*b*); – · – · –, linear approximation in H in (3.38*b*).

Because $-T_{0,xx}=-\phi_{0,xx}(x)\bar{T}_0(y)$, the solution for T_2^D is

$$T_2^D(x,y)=\phi_{0,xx}(x)T_2^{\perp}(x,y), \tag{3.36}$$

where

$$T_2^{\perp}(x,y) = \frac{y^3}{6}-\frac{1+Bi}{2Bi}y^2+\frac{Bi[Bi(f^3(x)-3f^2(x)+2)-3f^2(x)+6]+6}{6Bi(1+Bi-Bif(x))}(y-f(x)) - \frac{f^3(x)}{6}+\frac{1+Bi}{2Bi}f^2(x), \tag{3.37}$$

and

$$\phi_{0,xx}(x) = \frac{Bi(1+Bi)}{2H(1+Bi-Bif(x))^2}\left(f''(x)+\frac{2Bif'^2(x)}{1+Bi-Bif(x)}\right) \tag{3.38a}$$

$$\approx \frac{Bi}{2(1+Bi)}\hat{f}''(x)+\frac{Bi^2}{(1+Bi)^2}(\hat{f}(x)\hat{f}''(x)+\hat{f}'^2(x))H. \tag{3.38b}$$

Equation (3.38*a*) is approximated to (3.38*b*) by Taylor series expansions with respect to H around $H=0$ with retaining the terms up to the order of H. Figure 6 shows that the linear approximation in (3.38*b*) is reasonable.

As one can see from the first term in (3.38*b*), $\phi_{0,xx}(x)$ depends on $\hat{f}''(x)$, which is the normalised substrate 'curvature' and equal to $-\hat{f}(x)=-\sin x$ in this study, and the amplitude of the first term is $(1/2)Bi(1+Bi)^{-1}$. It should be emphasised that the dependence on $\hat{f}''(x)$ is caused by the horizontal diffusion of T_0. According to figure 6, the profile of $\phi_{0,xx}(x)$ can be roughly captured by the zeroth approximation in H. Consequently, $\phi_{0,xx}(x)$ contains the effect of substrate 'curvature' and the ratio of the internal to external heat transfer resistance of the liquid layer on T_2^D. The remaining linear contribution in H completes the $\phi_{0,xx}(x)$ profile.

A typical contour plot of T_2^D is shown in figure 7(*a*). At a specified x, $T_2^{\perp}$ causes T_2^D to change cubically along the vertical direction and the maximum $|T_2^D|$ to be located underneath the interface, as plotted in figure 7(*b*). Along the horizontal direction, the normalised substrate 'curvature' affects T_2^D, as indicated by $\phi_{0,xx}(x)$.

https://doi.org/10.1017/jfm.2018.812 Published online by Cambridge University Press

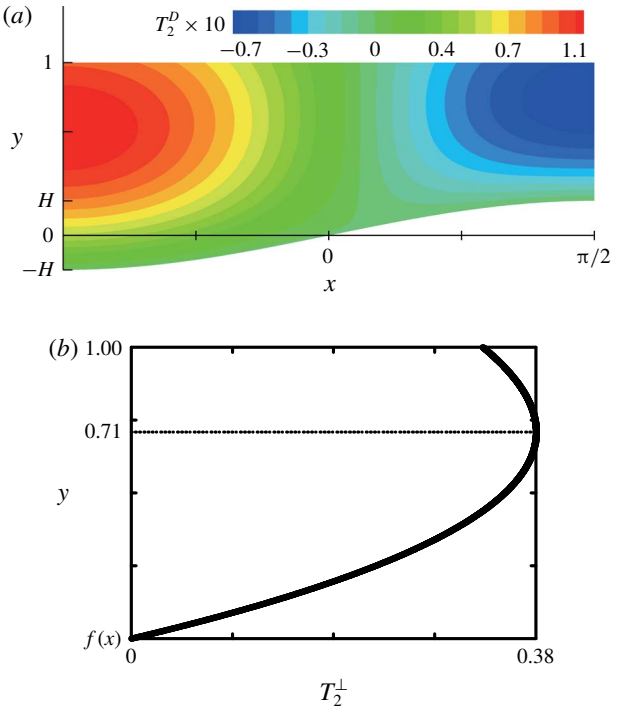


FIGURE 7. (Colour online) (*a*) Contour plot of T_2^D and (*b*) the plot of $T_2^\perp$ at $x = 0$. $Bi = 1$ and $H = 0.2$ for all plots.

The corresponding interfacial T_2^D profile becomes

$$T_2^D(x, 1) = \phi_{0,xx}(x) T_2^\perp(x, 1) \approx \frac{3 + Bi}{12(1 + Bi)^2} \hat{f}''(x) + \frac{1}{2(1 + Bi)^3} \left(\frac{Bi(3 + Bi)}{3} \hat{f}'^2(x) - \hat{f}(x) \hat{f}''(x) \right) H. \quad (3.39)$$

$\hat{f}''(x)$ in the first term of (3.39) indicates that $T_2^D(x, 1)$ may decrease in C_0. To check whether $T_2^D(x, 1)$ decreases or not, one needs to examine the sign of the interfacial T_2^D gradient.

The interfacial T_2^D gradient, $T_{2,x}^D|_{y=1}$, becomes

$$\Theta_2^{iD}(x) \approx \left(\frac{3 + Bi}{12(1 + Bi)^2} + \frac{Bi^2 + 3Bi - 3}{3(1 + Bi)^3} \hat{f}(x) H \right) \hat{f}'''(x). \quad (3.40)$$

The relationships $\hat{f}'''(x) = -\hat{f}'(x)$ and $\hat{f}''(x) = -\hat{f}(x)$ for the sinusoidal topography are used in (3.40). The $\Theta_2^{iD}(x)$ profile directly depends on $\hat{f}'''(x)$, which is equal to $-\hat{f}'(x) = -\cos x$ in this study. The term inside the parentheses becomes positive when

$$H < \frac{(Bi^2 + 4Bi + 3)}{4(Bi^2 + 3Bi - 3)}. \quad (3.41)$$

Under this condition, which is considered in this section, $\hat{f}'''(x)$ solely determines the sign of $\Theta_2^{iD}(x)$, and thus $\Theta_2^{iD}(x)$ is always negative in C_0. The sign of $\Theta_2^{iD}(x)$ is

https://doi.org/10.1017/jfm.2018.812 Published online by Cambridge University Press

opposite to that of $\Theta_0^i(x)$, which is proportional to $f'(x)$, as shown in (3.18*a*). Note that $\hat{f}'''(x)$ comes from the horizontal diffusion of T_0. For $Bi = 1$, any $0 < H < 1$ satisfies the condition in (3.41). For any Bi, $0 < H \leqslant 0.25$ satisfies the condition in (3.41). The other cases not satisfying (3.41) will be discussed in § 5.

The solution for T_2^C is

$$T_2^C(x, y) = Q_2(x, y) + \tilde{a}_2(x)y + \tilde{b}_2(x), \tag{3.42}$$

where

$$Q_2(x, y) = \int^{\xi} \int^{\xi} q_2(x, \xi)\, \mathrm{d}\xi\, \mathrm{d}\xi. \tag{3.43}$$

Here, we have introduced an integral notation $\int^{\xi} g(x, \xi)\, \mathrm{d}\xi$. The indefinite integral of $g(x, y)$ over y can be written as follows:

$$\int g(x, y)\, \mathrm{d}y = \int^{\xi} g(x, \xi)\, \mathrm{d}\xi + \alpha(x), \tag{3.44}$$

where $\alpha(x)$ is an arbitrary function of x. The notation represents the indefinite integral with $\alpha(x) = 0$. $Q_2(x, y)$, $\tilde{a}_2(x)$ and $\tilde{b}_2(x)$ are given by (A 1)–(A 7).

T_2^C is generated inside the liquid layer by the source term q_2. The magnitude of T_2^C is directly proportional to $\overline{Ma}$ because of the source term. Therefore, we examine the normalised $T_2^C/\overline{Ma}$ for simplicity to describe T_2^C. Figure 8(*a*) presents a contour plot of $T_2^C/\overline{Ma}$ for $Bi = 1$ and $H = 0.2$. The T_2^C contour plot is dramatically different from T_0; the vertical T_2^C gradient is not uniform along y, and the T_2^C profile does not follow the substrate shape. Among these differences, the interfacial T_2^C profile needs to be examined in detail, because it is likely to significantly contribute to the second correction for the flows via generating the interfacial ω_2. $T_0(x, 1)$ increases monotonically along the x direction in C_0, whereas $T_2^C(x, 1)$ changes non-monotonically; the minimum value appears at $x = -\pi/2$, but the maximum value is located at $x = x_m < \pi/2$ in C_0, as shown in figure 8(*b*).

Consequently, the interfacial T_2^C gradient, $T_{2,x}^C|_{y=1} = \Theta_2^{iC}(x)$, changes from positive to negative across $x = x_m$ in C_0 for $Bi = 1$ and $H = 0.2$. Here, we divide the interface into two regions: $-\pi/2 < x < x_m$ ($\Theta_2^{iC} > 0$), which shows a steep interfacial T_2^C gradient, and $x_m < x < \pi/2$ ($\Theta_2^{iC} < 0$), which exhibits a marginally decreasing $T_2^C(x, 1)$ profile. However, the non-monotonicity in $T_2^C(x, 1)$ vanishes, as Bi increases or H decreases. See figure 8(*b*). As Bi or H increases, the minimum value of $T_2^C(x, 1)$ increases and the maximum decreases, and then the magnitude of Θ_2^{iC} decreases.

To summarise, $A^2T_2 = A^2(T_2^D + T_2^C)$ is the second correction for the temperature field. The horizontal diffusion and the convection of T_0 cause $A^2T_2^D$ and $A^2T_2^C$, respectively. When figures 7(*a*) and 8(*a*) are compared with figure 3(*a*), in general, the horizontal diffusion of heat weakens the interfacial temperature gradient, and the convection of heat intensifies it. The interfacial T_2 gradient directly affects the second correction for the flows, which will be discussed in the next section.

3.2.2. *Flow field*

To the second correction, ω_2 and ψ_2 satisfy the governing equations

$$\omega_{2,yy} = -\omega_{0,xx} + \underbrace{\overline{Re}(\psi_{0,y}\omega_{0,x} - \psi_{0,x}\omega_{0,y})}_{=s_2(x,y)}, \tag{3.45}$$

$$\omega_2 = -\psi_{2,yy} - \psi_{0,xx}, \tag{3.46}$$

https://doi.org/10.1017/jfm.2018.812 Published online by Cambridge University Press

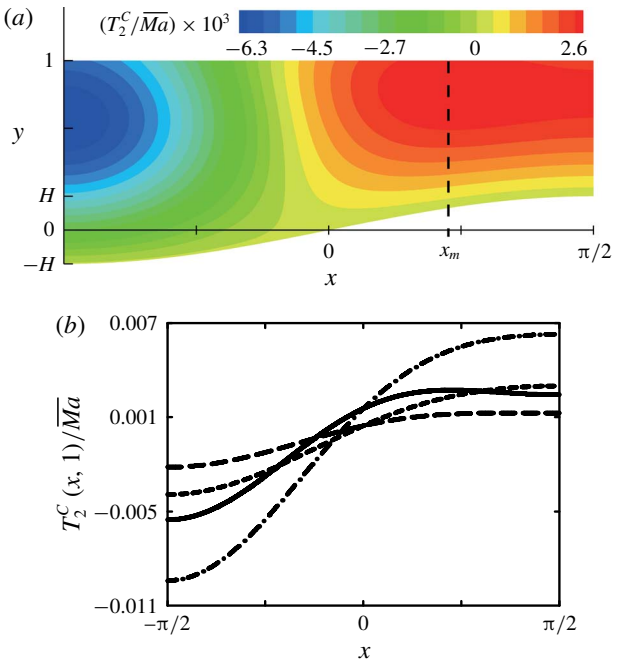


FIGURE 8. (Colour online) (*a*) Contour plot of $T_2^C/\overline{Ma}$ for $Bi = 1$ and $H = 0.2$, and (*b*) $T_2^C(x, 1)/\overline{Ma}$ profile corresponding to x: ——, $Bi = 1$, $H = 0.2$; — — —, $Bi = 2$, $H = 0.2$; – · – · –, $Bi = 1$, $H = 0.1$; – – – –, $Bi = 2$, $H = 0.1$.

together with the boundary conditions

$$\omega_2 = T_{2,x}, \quad \text{on } y = 1, \tag{3.47}$$

$$\psi_2 = \psi_{2,y} = 0, \quad \text{on } y = f(x), \tag{3.48}$$

where $\omega_2|_{y=1} = -u_{2,y}|_{y=1}$ in (3.47), and the condition of no net mass flow

$$\psi_2 = 0, \quad \text{on } y = 1. \tag{3.49}$$

$-\omega_{0,xx}$ is the term derived from the horizontal diffusion of ω_0, and s_2 is the term derived from the convection of ω_0 under the flows in the leading order.

The solutions satisfying the above set of equations can be split into homogeneous and particular parts, i.e. $\omega_2 = \omega_2^h + \omega_2^p$, $u_2 = u_2^h + u_2^p$ and $\psi_2 = \psi_2^h + \psi_2^p$, where the superscript h denotes the corresponding quantities in the homogeneous part, and p indicates those in the particular part. The problems for the homogeneous part are

$$\omega_{2,yy}^h = 0, \tag{3.50}$$

$$\omega_2^h = -\psi_{2,yy}^h, \tag{3.51}$$

$$\omega_2^h = T_{2,x}, \quad \text{on } y = 1, \tag{3.52}$$

$$\psi_2^h = \psi_{2,y}^h = 0, \quad \text{on } y = f(x), \tag{3.53}$$

$$\psi_2^h = 0, \quad \text{on } y = 1, \tag{3.54}$$

https://doi.org/10.1017/jfm.2018.812 Published online by Cambridge University Press

and the problems for the particular part are

$$\omega_{2,yy}^{p} = -\omega_{0,xx} + s_2, \tag{3.55}$$

$$\omega_2^{p} = -\psi_{2,yy}^{p} - \psi_{0,xx}, \tag{3.56}$$

$$\omega_2^{p} = 0, \quad \text{on } y = 1, \tag{3.57}$$

$$\psi_2^{p} = \psi_{2,y}^{p} = 0, \quad \text{on } y = f(x), \tag{3.58}$$

$$\psi_2^{p} = 0, \quad \text{on } y = 1. \tag{3.59}$$

The interfacial T_2 gradient, $T_{2,x}|_{y=1} = \Theta_2^i(x)$, is responsible for the generation of ω_2^h on the interface, as described by (3.52), and ω_2^h diffuses vertically. In the particular part, there are two source terms, $-\omega_{0,xx}$ and s_2, as described by (3.55). ω_2^p also propagates vertically.

The homogeneous solutions are

$$\begin{aligned}\omega_2^h(x, Y) &= \Theta_2^i(x)\bar{\omega}_0(Y) \\ &= \underbrace{\Theta_2^{iD}(x)\bar{\omega}_0(Y)}_{=\omega_2^{hD}(x,Y)} + \underbrace{\Theta_2^{iC}(x)\bar{\omega}_0(Y)}_{=\omega_2^{hC}(x,Y)},\end{aligned} \tag{3.60}$$

$$\begin{aligned}u_2^h(x, Y) &= \Theta_2^i(x)D(x)\bar{u}_0(Y) \\ &= \underbrace{\Theta_2^{iD}(x)D(x)\bar{u}_0(Y)}_{=u_2^{hD}(x,Y)} + \underbrace{\Theta_2^{iC}(x)D(x)\bar{u}_0(Y)}_{=u_2^{hC}(x,Y)},\end{aligned} \tag{3.61}$$

$$\begin{aligned}\psi_2^h(x, Y) &= \Theta_2^i(x)D^2(x)\bar{\psi}_0(Y) \\ &= \underbrace{\Theta_2^{iD}(x)D^2(x)\bar{\psi}_0(Y)}_{=\psi_2^{hD}(x,Y)} + \underbrace{\Theta_2^{iC}(x)D^2(x)\bar{\psi}_0(Y)}_{=\psi_2^{hC}(x,Y)}.\end{aligned} \tag{3.62}$$

This function splitting in (3.60)–(3.62) naturally appears because the governing equations are similar to those in the basic solutions. Unlike ω_0, however, the interfacial ω_2^h is generated by $\Theta_2^i(x) = \Theta_2^{iD}(x) + \Theta_2^{iC}(x)$. The homogeneous solutions are the linear combinations of two parts: $\omega_2^h = \omega_2^{hD} + \omega_2^{hC}$, $u_2^h = u_2^{hD} + u_2^{hC}$ and $\psi_2^h = \psi_2^{hD} + \psi_2^{hC}$, where superscripts hD and hC denote that the corresponding quantities concern $\Theta_2^{iD}(x)$ and $\Theta_2^{iC}(x)$, respectively.

The interfacial ω_2^{hD} is generated by $\Theta_2^{iD}(x)$ and diffuses throughout the layer vertically, as described by $\bar{\omega}_0(Y)$. $\Theta_2^{iD}(x)$ is the driving force for ω_2^{hD}, u_2^{hD} and ψ_2^{hD}, and (3.40) indicates that $\Theta_2^{iD}(x)$ has the sign opposite to that of $\Theta_0^i(x)$. Therefore, the direction of recirculation, as shown in figure 9, is opposite to that in the basic solutions, as shown in figure 5.

The interfacial ω_2^{hC} is generated by $\Theta_2^{iC}(x)$, and it diffuses vertically again. $\Theta_2^{iC}(x)$ is the driving force for ω_2^{hC}, u_2^{hC} and ψ_2^{hC}. The linear dependence of T_2^C on $\overline{Ma}$ is transferred to the solutions via $\Theta_2^{iC}(x)$. Figure 10 presents the contour plots of $\omega_2^{hC}/\overline{Ma}$, $u_2^{hC}/\overline{Ma}$ and $\psi_2^{hC}/\overline{Ma}$ for $Bi = 1$ and $H = 0.2$. The non-monotonic $T_2^C(x, 1)$ profile leads to the anticlockwise recirculation for R^+ region ($-\pi/2 < x < x_m$) and the clockwise recirculation for R^- region ($x_m < x < \pi/2$), and the recirculation is stronger inside R^+ than that inside R^-, as the sign and the magnitude of the driving force $\Theta_2^{iC}(x)$ are transferred inside via the vertical diffusion. Additionally, the vertical diffusion clearly explains why the boundary between R^+ and R^- is a straight line, i.e. $x = x_m$ in figure 10. When Bi increases or H decreases, positive Θ_2^{iC} along the

https://doi.org/10.1017/jfm.2018.812 Published online by Cambridge University Press

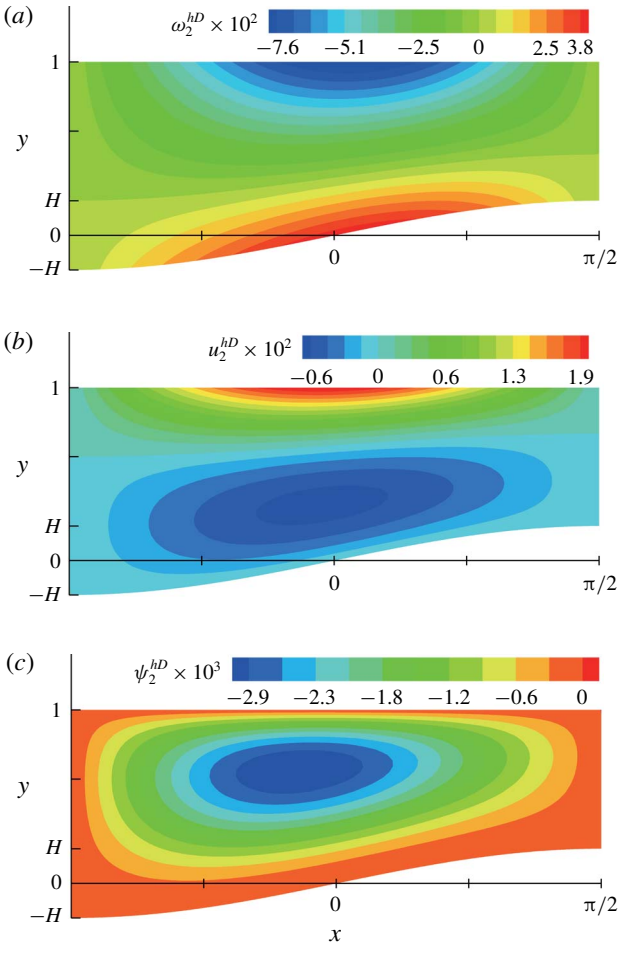


FIGURE 9. (Colour online) Contour plots of (*a*) ω_2^{hD}, (*b*) u_2^{hD} and (*c*) ψ_2^{hD} for $Bi = 1$ and $H = 0.2$.

entire interface causes only the anticlockwise recirculation in C_0, which implies the R^- region disappears.

The particular solutions are also the linear combinations of two parts: $\omega_2^p = -(\psi_{2,yy}^{pD} + \psi_{0,xx}) - \psi_{2,yy}^{pC}$, $u_2^p = u_2^{pD} + u_2^{pC}$ and $\psi_2^p = \psi_2^{pD} + \psi_2^{pC}$, where the superscripts pD and pC denote that the corresponding quantities arise from the source terms $-\omega_{0,xx}$ and s_2, respectively. Unlike the homogeneous solutions, ω_2^p, u_2^p and ψ_2^p are generated inside the liquid layer by the source terms. They are

$$\omega_2^p(x, y) = \underbrace{Z_{2,yy}(x, y) - \tilde{c}_2^{pD}(x)y - \tilde{d}_2^{pD}(x)}_{=-\psi_{2,yy}^{pD}(x,y)} - \psi_{0,xx}(x, y) + \underbrace{S_{2,yy}(x, y) - \tilde{c}_2^{pC}(x)y - \tilde{d}_2^{pC}(x)}_{=-\psi_{2,yy}^{pC}(x,y)}, \tag{3.63}$$

https://doi.org/10.1017/jfm.2018.812 Published online by Cambridge University Press

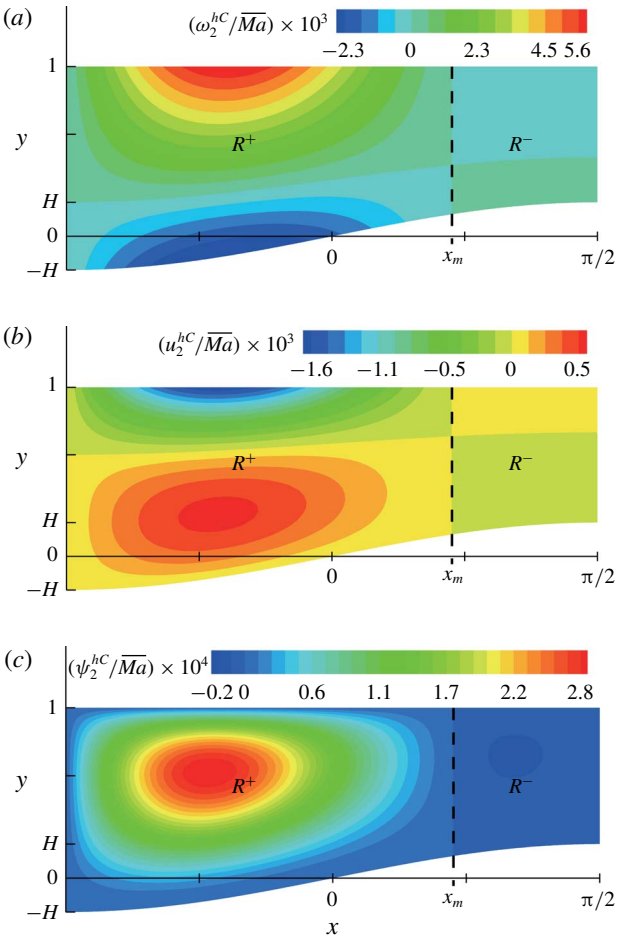


FIGURE 10. (Colour online) Contour plots of (*a*) $\omega_2^{hC}/\overline{Ma}$, (*b*) $u_2^{hC}/\overline{Ma}$ and (*c*) $\psi_2^{hC}/\overline{Ma}$ for $Bi = 1$ and $H = 0.2$.

$$u_2^p(x,y) = \underbrace{-Z_{2,y}(x,y) + \frac{\tilde{c}_2^{pD}(x)}{2}y^2 + \tilde{d}_2^{pD}(x)y + \tilde{e}_2^{pD}(x)}_{=u_2^{pD}(x,y)}$$
$$\underbrace{-S_{2,y}(x,y) + \frac{\tilde{c}_2^{pC}(x)}{2}y^2 + \tilde{d}_2^{pC}(x)y + \tilde{e}_2^{pC}(x)}_{=u_2^{pC}(x,y)}, \tag{3.64}$$

$$\psi_2^p(x,y) = \underbrace{-Z_2(x,y) + \frac{\tilde{c}_2^{pD}(x)}{6}y^3 + \frac{\tilde{d}_2^{pD}(x)}{2}y^2 + \tilde{e}_2^{pD}(x)y + \tilde{f}_2^{pD}(x)}_{=\psi_2^{pD}(x,y)}$$
$$\underbrace{-S_2(x,y) + \frac{\tilde{c}_2^{pC}(x)}{6}y^3 + \frac{\tilde{d}_2^{pC}(x)}{2}y^2 + \tilde{e}_2^{pC}(x)y + \tilde{f}_2^{pC}(x)}_{=\psi_2^{pC}(x,y)}, \tag{3.65}$$

https://doi.org/10.1017/jfm.2018.812 Published online by Cambridge University Press

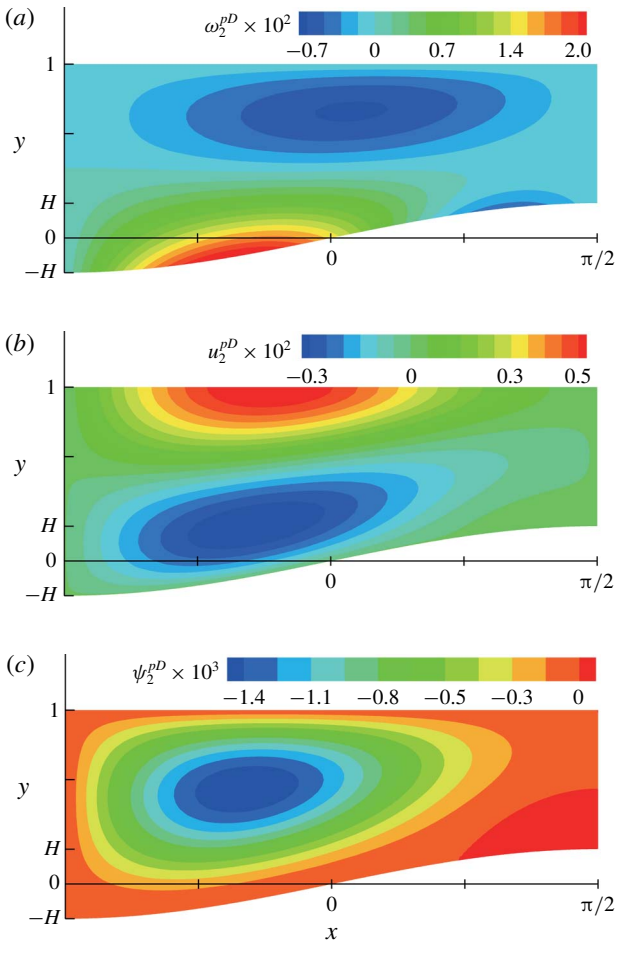


FIGURE 11. (Colour online) Contour plots of (*a*) ω_2^{pD}, (*b*) u_2^{pD} and (*c*) ψ_2^{pD} for $Bi = 1$ and $H = 0.2$.

where

$$Z_2(x, y) = \int^{\xi}\int^{\xi}\int^{\xi}\int^{\xi} (-\omega_{0,xx}(x, \xi) + \psi_{0,xx\xi\xi}(x, \xi))\, \mathrm{d}\xi\, \mathrm{d}\xi\, \mathrm{d}\xi\, \mathrm{d}\xi, \tag{3.66}$$

$$S_2(x, y) = \int^{\xi}\int^{\xi}\int^{\xi}\int^{\xi} s_2(x, \xi)\, \mathrm{d}\xi\, \mathrm{d}\xi\, \mathrm{d}\xi\, \mathrm{d}\xi. \tag{3.67}$$

$Z_2(x, y)$, $S_2(x, y)$, $\tilde{c}_2^{pD}(x)$, $\tilde{c}_2^{pC}(x)$, $\tilde{d}_2^{pD}(x)$, $\tilde{d}_2^{pC}(x)$, $\tilde{e}_2^{pD}(x)$, $\tilde{e}_2^{pC}(x)$, $\tilde{f}_2^{pD}(x)$, $\tilde{f}_2^{pC}(x)$ and $\psi_{0,xx}(x, y)$ are given by (A 8)–(A 26).

Figure 11 shows $\omega_2^{pD} = -(\psi_{2,yy}^{pD} + \psi_{0,xx})$, u_2^{pD} and ψ_2^{pD} for $Bi = 1$ and $H = 0.2$. They behave similarly to ω_2^{hD}, u_2^{hD} and ψ_2^{hD} in figure 9, which implies both the quantities with superscripts hD and pD cause the recirculation counter-rotation to the vortex in the basic solutions and weaken the overall flow. The similarity probably arises from the common term $\phi_{0,xxx}(x)$. For the quantities with hD, $\phi_0(x)$ in T_0 is differentiated two times with respect to x via the horizontal diffusion of T_0 for T_2^D and once

https://doi.org/10.1017/jfm.2018.812 Published online by Cambridge University Press

again via obtaining interfacial T_2^D gradient. For the quantities with pD, $\phi_0(x)$ in T_0 is differentiated once with respect to x via obtaining interfacial T_0 gradient for ω_0 and two times again via the horizontal diffusion of ω_0. Therefore, $\phi_{0,xxx}(x)$ naturally appears in all the quantities. However, the magnitudes of the quantities with pD are smaller than those of the quantities with hD. One can understand ω_2^{pD}, u_2^{pD} and ψ_2^{pD} make a minor contribution to weakening the overall flow, whereas the quantities with hD make the major contribution.

With the parameter set of $Bi = 1$ and $H = 0.2$, the maximum values of $|-\psi_{2,yy}^{pC}|$, $|u_2^{pC}|$ and $|\psi_2^{pC}|$ are estimated to be $1.89\overline{Re} \times 10^{-4}$, $5.29\overline{Re} \times 10^{-5}$ and $1.37\overline{Re} \times 10^{-5}$, respectively. This implies that the contributions of the source term s_2 are not significant in the second-order solutions for a typical fluid, of which Pr is generally $O(1)$ or higher.

To summarise, $A^2\omega_2 = A^2(\omega_2^{hD} + \omega_2^{hC} + \omega_2^{pD} + \omega_2^{pC})$ is the second correction for the flows. The horizontal diffusion and the convection of T_0 cause $A^2\Theta_2^{iD}(x)$ and $A^2\Theta_2^{iC}(x)$, and they are responsible for the behaviours of $A^2\omega_2^{hD}$ and $A^2\omega_2^{hC}$ as the driving forces, respectively. When figures 9 and 10 are compared with figure 5, in general, the horizontal diffusion of heat weakens and the convection of heat intensifies the overall flow. In addition, the horizontal diffusion of ω_0 affects $A^2\omega_2^{pD}$, which makes a minor contribution to weakening the overall flow, and the convection of ω_0 induces $A^2\omega_2^{pC}$, which is insignificant in the second-order solution under the conditions used in this study.

3.3. *Interfacial vorticity*

The vertical diffusion of the interfacial vorticity mainly governs the thermocapillary flows in this study. Therefore, the magnitude of the interfacial vorticity can be a representative quantity for the intensity of the flows. The contributions from the convection and the diffusion to the flows can be indirectly measured by the amount of interfacial vorticity from them.

The vorticity is represented by the second-order solution

$$\omega = \omega_0 + A^2(\omega_2^{hD} + \omega_2^{hC} + \omega_2^{pD} + \omega_2^{pC}) + O(A^3). \tag{3.68}$$

According to our analysis, the vertical diffusion of the interfacial vorticity in the leading order is the dominant factor in generating the flows. Therefore, the intensity of the flows can be characterised by the interfacial ω_0

$$\omega_0(x, 1) = \Theta_0^i(x). \tag{3.69}$$

The magnitude of $\Theta_0^i(x)$ can be approximated by $(\delta T_0|_{y=1})/\delta x$, where $\delta T|_{y=1} = T(\pi/2, 1) - T(-\pi/2, 1)$ in C_0, and $\delta x = \pi$ is the horizontal size of the unit cell. Using (3.13), $(\delta T_0|_{y=1})/\delta x$ is given by

$$\frac{\delta T_0|_{y=1}}{\delta x} = \frac{1 + Bi}{\pi[(1 + Bi)^2 - Bi^2H^2]}. \tag{3.70}$$

In the second correction, $A^2\omega_2^{hD}$ and $A^2\omega_2^{hC}$ are caused by the vertical diffusion of the interfacial $A^2\omega_2$, whereas $A^2\omega_2^{pD}$ and $A^2\omega_2^{pC}$ are caused by the vertical diffusion of the generated vorticity inside the liquid layer. $A^2\omega_2^{hD}$ and $A^2\omega_2^{pD}$ show the effect of the horizontal diffusion of heat and vorticity, respectively, on the overall flow.

https://doi.org/10.1017/jfm.2018.812 Published online by Cambridge University Press

As discussed in the previous section, $A^2\omega_2^{pD}$ makes a minor contribution to weakening the overall flow by horizontal diffusion. Therefore, the horizontal diffusion effect can be understood by considering the interfacial $A^2\omega_2^{hD}$:

$$A^2\omega_2^{hD}(x,1) = A^2\Theta_2^{iD}(x). \tag{3.71}$$

Using (3.36), the magnitude of $\Theta_2^{iD}(x)$ is approximated by

$$\frac{\delta T_2^D|_{y=1}}{\delta x} = -\frac{1+Bi}{12\pi}\left\{\frac{[3+Bi(1-H)](1-H)^2}{[1+Bi(1-H)]^3} + \frac{[3+Bi(1+H)](1+H)^2}{[1+Bi(1+H)]^3}\right\}. \tag{3.72}$$

$A^2\omega_2^{hC}$ and $A^2\omega_2^{pC}$ in the second correction show the effect of the convection of heat and vorticity, respectively, on the overall flow. Because $A^2\omega_2^{pC}$ is insignificant, the effect can be captured by the interfacial $A^2\omega_2^{hC}$:

$$A^2\omega_2^{hC}(x,1) = A^2\Theta_2^{iC}(x). \tag{3.73}$$

Moreover, using (3.42), the magnitude of $\Theta_2^{iC}(x)$ is approximated by

$$\frac{\delta T_2^C|_{y=1}}{\delta x} = \frac{Ma(1+Bi)^2}{320\pi H}\left(\left(\frac{1-H}{1+Bi-BiH}\right)^4 + \left(\frac{1+H}{1+Bi+BiH}\right)^4\right). \tag{3.74}$$

4. Numerical validation

In this section, we solve the heat, momentum and mass balance equations directly to find the field variables, i.e. T, u, v and p, for two-dimensional steady thermocapillary flows over a heated substrate with sinusoidal topography. These equations are discretised and solved by a standard technique of the Galerkin finite element method (G/FEM) (Becker, Carey & Oden 1981; Zienkiewicz & Taylor 2000). Note that the equations of the system are fully coupled, which means all equations are solved at once.

Since the gas/liquid interface disturbance is insignificant, the interface is assumed to be flat. After a suitable scaling with (2.24), the governing equations (2.4)–(2.7) and the boundary conditions (2.12)–(2.15) are translated into the primitive variables:

$$MaA(uT_x + vT_y) = A^2T_{xx} + T_{yy}, \tag{4.1}$$

$$ReA(uu_x + vu_y) = -p_x + A^2u_{xx} + u_{yy}, \tag{4.2}$$

$$ReA^3(uv_x + vv_y) = -p_y + A^4v_{xx} + A^2v_{yy}, \tag{4.3}$$

$$u_x + v_y = 0, \tag{4.4}$$

and

$$T_y = -BiT - \frac{1}{2H}, \quad \text{on } y=1, \tag{4.5}$$

$$T = \frac{1}{2H}, \quad \text{on } y=f(x), \tag{4.6}$$

$$\left.\begin{array}{c} u_y = -T_x, \\ v = 0, \end{array}\right\} \quad \text{on } y=1, \tag{4.7}$$

$$u = v = 0, \quad \text{on } y=f(x). \tag{4.8}$$

Note that the normal stress condition becomes trivial for the flat interface. The flow domain for the finite element computation covers four unit cells, which correspond to two periods of $f(x)$ around $x=0$ from $x=-2\pi$ to $x=2\pi$. The choice of the

https://doi.org/10.1017/jfm.2018.812 Published online by Cambridge University Press

(*a*) $Bi=1,\ H=0.1$			(*b*) $Bi=1,\ H=0.2$		
	Basic	Second-order		Basic	Second-order
T	9.38×10^{-4}	4.76×10^{-6}	T	1.07×10^{-3}	4.41×10^{-6}
u	2.33×10^{-4}	6.56×10^{-7}	u	2.51×10^{-4}	9.35×10^{-7}
(*c*) $Bi=2,\ H=0.1$			(*d*) $Bi=2,\ H=0.2$		
	Basic	Second-order		Basic	Second-order
T	6.62×10^{-4}	3.81×10^{-6}	T	7.40×10^{-4}	3.23×10^{-6}
u	1.36×10^{-4}	3.34×10^{-7}	u	1.43×10^{-4}	4.31×10^{-7}
(*e*) $Bi=0.5,\ H=0.1$			(*f*) $Bi=0.5,\ H=0.2$		
	Basic	Second-order		Basic	Second-order
T	1.33×10^{-3}	6.10×10^{-6}	T	1.56×10^{-3}	6.51×10^{-6}
u	3.52×10^{-4}	1.19×10^{-6}	u	3.99×10^{-4}	1.99×10^{-6}

TABLE 1. The maximum discrepancies between the asymptotic solutions (the basic or the second-order solutions) and the numerical solutions for T and u, respectively. $Ma=0.1$, $Re=0.1$ and $A=0.1$ for all cases.

domain larger than one unit cell is to check the symmetric and periodic structures of the numerical solutions. Because of the periodicity, we impose the periodic boundary condition on the side walls at $x=-2\pi$ and $x=2\pi$.

The domain is tessellated by nine-node quadrilateral elements, and 36 000 elements and 146 461 nodes are used in this study. Each field variable is approximated by a linear combination of a finite number of basis functions, which are the unknowns of the discretised problem. The temperature and velocity fields are represented in terms of Lagrangian biquadratic functions and the pressure in terms of Lagrangian linear functions. The weak forms of the governing equations (4.1)–(4.4) are obtained by multiplying with weighting functions, integrating over the physical domain, and applying the divergence theorem to the appropriate terms. Essential boundary conditions are imposed by replacing the corresponding weighted residual equation with the desired velocity or temperature specification. Natural boundary conditions are applied through the boundary integrals that come from the divergence theorem. The G/FEM reduces the governing equations to a set of nonlinear algebraic equations on the basis function coefficients. These equations are solved iteratively by Newton's method. The iteration continues until the L^2-norms of both the solution update vector and the weighted residual vector fall below 10^{-8}.

For the justification of computations using steady equations (4.1)–(4.4), the full transient computations are performed under the characteristic time scale $(\lambda/2\pi)A^3/U$. Herein, the time-dependent terms $Ma\,A^{-2}T_t$, $Re\,A^{-2}u_t$ and $Re\,v_t$ are added to the left-hand sides of (4.1), (4.2) and (4.3), respectively. The nominal steady-state flows can be reached within time $t=50$ according to the results using the backward Euler scheme with the time step $\Delta t=0.1$ and the initial conditions $T=u=v=0$ for the cases described in table 1. The maximum value of the horizontal velocity $|u|_{max}$ is used to demonstrate that the flows settle down to the steady state. For the system parameter used in table 1(*b*), $|u|_{max}$ over t is depicted in figure 12. Furthermore, the steady-state values of the primitive variables computed from the full transient equations are

https://doi.org/10.1017/jfm.2018.812 Published online by Cambridge University Press

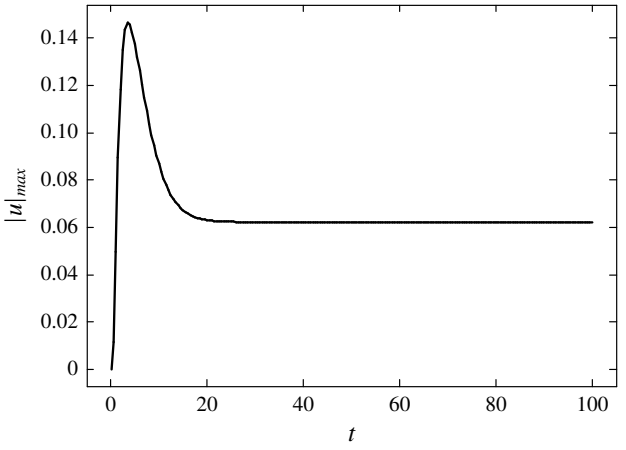


FIGURE 12. $|u|_{max}$ over t for $Ma = 0.1$, $Re = 0.1$, $Bi = 1$, $A = 0.1$ and $H = 0.2$.

virtually indistinguishable from those from the steady-state equations (4.1)–(4.4). The same conclusions are drawn from the other cases. Therefore, the steady-state equations are suitable for examining the flows considered in this study.

The maximum discrepancies between the asymptotic solutions (the basic or the second-order solutions) and the numerical solutions from G/FEM are estimated for T and u, respectively. $Ma = 0.1$, $Re = 0.1$ and $A = 0.1$ are fixed, and Bi and H vary, as shown in table 1. The maximum discrepancies are summarised in table 1. The discrepancies with the second-order solutions are insignificant, and they are much smaller than those with the basic solutions. This strongly suggests that the predictions from the second-order solutions are valid for the parameters considered in this study.

In addition, the results are qualitatively compared with the predictions by using the volume of fluid (VOF) method (Alexeev *et al.* 2005). Note that the reported numerical results are predicted under higher Marangoni and capillary numbers compared with this study. Such conditions induce strong flows near the interface and weak capillary action that may be not favourable to maintain a flat interface. However, according to their results, the shape of the interface is virtually flat, as shown in figure 8(*a*) of Alexeev *et al.* (2005). Also, the similar behaviours, with respect to the number of vortices and direction of recirculation, have been reported.

5. Final remarks

Thermocapillary flows over the uniformly heated substrate with sinusoidal topography are considered by asymptotic theory. The temperature and flow fields are analysed with second-order solutions for small A. Heating by the substrate, horizontal diffusion and convection contribute to the temperature and flow fields.

The effects of Bi and H are adequately described by (3.70). As Bi increases, the interfacial temperature gradient decreases, and hence weak flow ensues; weak vortices are caused by strong cooling by a gas. As H increases, the interfacial temperature gradient increases, and hence strong flow ensues; strong vortices are caused by a large difference in the vertical heat fluxes between the interface above the trough and the crest of the substrate, as indicated by equation (3.15). Those speculations are valid when $Bi = O(1)$ and $H = O(0.1)$, as defined in this study.

https://doi.org/10.1017/jfm.2018.812 Published online by Cambridge University Press

The horizontal diffusion weakens the overall flow. Note the minus sign in (3.72). The convection intensifies the overall flow, as shown in (3.74). The effect of the convection is directly proportional to Ma, whereas the effect of the horizontal diffusion is consistent for a specified topography. The significant contributions of the horizontal diffusion and convection are expected when A increases within small A limit.

The upper limit of H is considered, as indicated by (3.41). When not satisfying (3.41), i.e.

$$H > \frac{(Bi^2 + 4Bi + 3)}{4(Bi^2 + 3Bi - 3)}, \tag{5.1}$$

the term inside the parentheses in (3.40) is not positive along the entire interface. The term can be negative near the interface above the trough of the substrate, but it becomes positive in the other region. Thus, under that condition, $\Theta_2^{iD}(x)$ also has positive values near the interface above the trough in C_0, which generates the anticlockwise recirculation in that region. However, even if the anticlockwise recirculation appears, equation (3.40) provides that another stronger clockwise recirculation appears next to the anticlockwise one in the unit cell, which implies the horizontal diffusion of heat still contributes to weakening the overall flow.

The analysis of the asymptotic solutions is based on the sinusoidal function $f(x)$, but any function can be applied to $f(x)$. Heat and flow behaviours over various substrates can be investigated by the results derived in this study.

Whereas many aspects of the thermocapillary flows over the substrate with sinusoidal topography, such as the influence of the system parameters, are understood, a number of points need a deeper investigation. We wish to remark that three-dimensional flows are worth studying to apply various topographies such as a pyramid-shape that has periodicity in the in-plane directions. Moreover, interface disturbance should be considered for higher Ca.

Acknowledgements

This work was supported by the National Research Foundation of Korea (NRF) grant funded by the Korea government (MSIT) (nos NRF-2018R1A5A1024127 and NRF-2016R1D1A1B03931632).

Appendix A

$Q_2(x, y)$ in (3.43) is given by

$$Q_2(x, y) = -\frac{\overline{Ma}(1 + Bi)^2}{960H^2(1 - f(x))^2(1 + Bi - Bif(x))^4} \times (\tilde{A}(x)y^5 + \tilde{B}(x)y^4 + \tilde{C}(x)y^3 + \tilde{D}(x)y^2), \tag{A 1}$$

where

$$\tilde{A}(x) = 3(1 - f(x))(1 + Bi - Bif(x))f''(x) + 3f'^2(x), \tag{A 2}$$

$$\tilde{B}(x) = -5(1 + 2f(x))(1 - f(x))(1 + Bi - Bif(x))f''(x) - 15f(x)f'^2(x), \tag{A 3}$$

$$\tilde{C}(x) = 10(2 + f(x))(1 - f(x))(1 + Bi - Bif(x))f(x)f''(x) + 30f^2(x)f'^2(x), \tag{A 4}$$

$$\tilde{D}(x) = -30(1 - f(x))(1 + Bi - Bif(x))f^2(x)f''(x) - 30f^3(x)f'^2(x). \tag{A 5}$$

https://doi.org/10.1017/jfm.2018.812 Published online by Cambridge University Press

$\tilde{a}_2(x)$ and $\tilde{b}_2(x)$ in (3.42) are defined by

$$\tilde{a}_2(x) = -\frac{Q_{2,y}(x,\,1) + Bi\,Q_2(x,\,1) - Bi\,Q_2(x, f(x))}{1 + Bi - Bif(x)}, \tag{A 6}$$

$$\tilde{b}_2(x) = -Q_2(x, f(x)) - \tilde{a}_2(x)f(x). \tag{A 7}$$

$Z_2(x, y)$ in (3.66) is given by

$$Z_2(x, y) = -\frac{1 + Bi}{48H(1 - f(x))^3(1 + Bi - Bif(x))^4}(\tilde{E}(x)y^5 + \tilde{F}(x)y^4), \tag{A 8}$$

where

$$\begin{aligned}\tilde{E}(x) \;=\; & \tfrac{6}{5}[1 + 4Bi + 6Bi^2 - 4Bi(1 + 3Bi)f(x) + 6Bi^2f^2(x)]f'^3(x) \\ & + \tfrac{9}{5}(1 + 3Bi - 3Bif(x))(1 - f(x))(1 + Bi - Bif(x))f'(x)f''(x) \\ & + \tfrac{3}{5}(1 - f(x))^2(1 + Bi - Bif(x))^2f'''(x), \end{aligned} \tag{A 9}$$

$$\begin{aligned}\tilde{F}(x) \;=\; & -6[(1 + 2Bi)^2 - 2Bi(2 + 3Bi)f(x) + 2Bi^2f^3(x)]f'^3(x) \\ & - 3(3 + 5Bi - Bif(x) - 4Bif^2(x))(1 - f(x))(1 + Bi - Bif(x))f'(x)f''(x) \\ & - (1 + 2f(x))(1 - f(x))^2(1 + Bi - Bif(x))^2f'''(x). \end{aligned} \tag{A 10}$$

$S_2(x, y)$ in (3.67) is given by

$$S_2(x, y) = \frac{\overline{Re}(1 + Bi)^2f'(x)}{1920H^2(1 - f(x))^3(1 + Bi - Bif(x))^5} \times (\tilde{G}(x)y^7 + \tilde{H}(x)y^6 + \tilde{I}(x)y^5 + \tilde{J}(x)y^4), \tag{A 11}$$

where

$$\tilde{G}(x) = -\tfrac{3}{7}[(1 - f(x))(1 + Bi - Bif(x))f''(x) + (1 + 3Bi - 3Bif(x))f'^2(x)], \tag{A 12}$$

$$\tilde{H}(x) = (1 + 2f(x))[(1 - f(x))(1 + Bi - Bif(x))f''(x) + (1 + 3Bi - 3Bif(x))f'^2(x)], \tag{A 13}$$

$$\begin{aligned}\tilde{I}(x) \;=\; & -[2Bi + 6(1 + 2Bi)f(x) + 3(1 - Bi)f^2(x) - 11Bif^3(x)]f'^2(x) \\ & - (1 + 2f(x))^2(1 - f(x))(1 + Bi - Bif(x))f''(x), \end{aligned} \tag{A 14}$$

$$\begin{aligned}\tilde{J}(x) \;=\; & 5f(x)\{(1 - f^3(x))(1 + Bi - Bif(x))f''(x) \\ & + [2Bi + 3(1 + Bi)f(x) - 3Bif^2(x) - 2Bif^3(x)]f'^2(x)\}. \end{aligned} \tag{A 15}$$

$\tilde{c}_2^{pD}(x)$, $\tilde{c}_2^{pC}(x)$, $\tilde{d}_2^{pD}(x)$, $\tilde{d}_2^{pC}(x)$, $\tilde{e}_2^{pD}(x)$, $\tilde{e}_2^{pC}(x)$, $\tilde{f}_2^{pD}(x)$, $\tilde{f}_2^{pC}(x)$ in (3.63)–(3.65) are defined by

$$\tilde{c}_2^{pD}(x) = \frac{3}{2(1 - f(x))}Z_{2,yy}(x,\,1) + \frac{3}{(1 - f(x))^2}\left(Z_{2,y}(x, f(x)) - \frac{Z_2(x,\,1) - Z_2(x, f(x))}{1 - f(x)}\right), \tag{A 16}$$

$$\tilde{c}_2^{pC}(x) = \frac{3}{2(1 - f(x))}S_{2,yy}(x,\,1) + \frac{3}{(1 - f(x))^2}\left(S_{2,y}(x, f(x)) - \frac{S_2(x,\,1) - S_2(x, f(x))}{1 - f(x)}\right), \tag{A 17}$$

$$\tilde{d}_2^{pD}(x) = Z_{2,yy}(x,\,1) - \tilde{c}_2^{pD}(x), \tag{A 18}$$

$$\tilde{d}_2^{pC}(x) = S_{2,yy}(x,\,1) - \tilde{c}_2^{pC}(x), \tag{A 19}$$

https://doi.org/10.1017/jfm.2018.812 Published online by Cambridge University Press

$$\tilde{e}_2^{pD}(x) = Z_{2,y}(x, f(x)) - Z_{2,yy}(x, 1)f(x) - \frac{\tilde{c}_2^{pD}(x)(f^2(x) - 2f(x))}{2}, \tag{A 20}$$

$$\tilde{e}_2^{pC}(x) = S_{2,y}(x, f(x)) - S_{2,yy}(x, 1)f(x) - \frac{\tilde{c}_2^{pC}(x)(f^2(x) - 2f(x))}{2}, \tag{A 21}$$

$$\tilde{f}_2^{pD}(x) = Z_2(x, 1) - \frac{\tilde{c}_2^{pD}(x)}{6} - \frac{\tilde{d}_2^{pD}(x)}{2} - \tilde{e}_2^{pD}(x), \tag{A 22}$$

$$\tilde{f}_2^{pC}(x) = S_2(x, 1) - \frac{\tilde{c}_2^{pC}(x)}{6} - \frac{\tilde{d}_2^{pC}(x)}{2} - \tilde{e}_2^{pC}(x). \tag{A 23}$$

$\psi_{0,xx}(x, y)$ in (3.63) is given by

$$\psi_{0,xx}(x, y) = \frac{(1 + Bi)(1 - y)}{8H(1 - f(x))^3(1 + Bi - Bif(x))^4}(\tilde{K}(x, y) + \tilde{L}(x, y)), \tag{A 24}$$

where

$$\begin{aligned}\tilde{K}(x, y) \;=\; & [(2 + 5Bi - 5Bif(x))y - 1 - Bi - (1 + 3Bi)f(x) + 4Bif^2(x)]f'(x) \\ & \times \{(1 - f(x))(1 + Bi - Bif(x))(y - f(x))f''(x) \\ & + [(1 + 3Bi - 3Bif(x))y - 2 - 2Bi + (1 + Bi)f(x) + Bif^2(x)]f'^2(x)\},\end{aligned} \tag{A 25}$$

$$\begin{aligned}\tilde{L}(x, y) \;=\; & (1 - f(x))(1 + Bi - Bif(x))(y - f(x)) \\ & \times \{(1 - f(x))(1 + Bi - Bif(x))(y - f(x))f'''(x) \\ & + (-3Bi\, y + 1 + Bi + 2Bif(x))f'^3(x) \\ & + [(1 + 4Bi - 4Bif(x))y - 5 - 5Bi + (4 + 6Bi)f(x) - Bif^2(x)]f'(x)f''(x)\}.\end{aligned} \tag{A 26}$$

REFERENCES

ALEXEEV, A., GAMBARYAN-ROISMAN, T. & STEPHAN, P. 2005 Marangoni convection and heat transfer in thin liquid films on heated walls with topography: experiments and numerical study. *Phys. Fluids* **17**, 062106.

BECKER, E. B., CAREY, G. F. & ODEN, J. T. 1981 *Finite Elements: An Introduction*. Prentice-Hall.

BIRIKH, R. V. 1966 Thermocapillary convection in a horizontal layer of liquid. *J. Appl. Mech. Tech. Phys.* **7**, 43–44.

CORMACK, D. E., LEAL, L. G. & IMBERGER, J. 1974 Natural convection in a shallow cavity with differentially heated end walls. Part 1. Asymptotic theory. *J. Fluid Mech.* **65**, 209–229.

CUVELIER, C. & DRIESSEN, J. M. 1986 Thermocapillary free boundaries in crystal growth. *J. Fluid Mech.* **169**, 1–26.

ECKERT, K., BESTEHORN, M. & THESS, A. 1998 Square cells in surface-tension-driven Bénard convection: experiment and theory. *J. Fluid Mech.* **356**, 155–197.

EVANS, P. L. & MÜNCH, A. 2006 Interaction of advancing fronts and meniscus profiles formed by surface-tension-gradient-driven liquid films. *SIAM J. Appl. Maths* **66**, 1610–1631.

FATH, A., HORN, T., GAMBARYAN-ROISMAN, T., STEPHAN, P. & BOTHE, D. 2015 Numerical and experimental analysis of short-scale Marangoni convection on heated structured surfaces. *Intl J. Heat Mass Transfer* **86**, 764–779.

FRUMKIN, V. & ORON, A. 2016 Liquid film flow along a substrate with an asymmetric topography sustained by the thermocapillary effect. *Phys. Fluids* **28**, 082107.

GAMBARYAN-ROISMAN, T., ALEXEEV, A. & STEPHAN, P. 2005 Effect of the microscale wall topography on the thermocapillary convection within a heated liquid film. *Exp. Therm. Fluid Sci.* **29**, 765–772.

https://doi.org/10.1017/jfm.2018.812 Published online by Cambridge University Press

GAMBARYAN-ROISMAN, T. & STEPHAN, P. 2007 Thermocapillary convection and interface deformation in a liquid film within a micro-slot with structured walls. *Microfluid. Nanofluid.* **3**, 207–215.

GERI, M., KESHAVARZ, B., MCKINLEY, G. H. & BUSH, J. W. M. 2017 Thermal delay of drop coalescence. *J. Fluid Mech.* **833**, R3.

GUPTA, A., SBRAGAGLIA, M., BELARDINELLI, D. & SUGIYAMA, K. 2016 Lattice Boltzmann simulations of droplet formation in confined channels with thermocapillary flows. *Phys. Rev.* E **94**, 063302.

ISMAGILOV, R. F., ROSMARIN, D., GRACIAS, D. H., STROOCK, A. D. & WHITESIDES, G. M. 2001 Competition of intrinsic and topographically imposed patterns in Bénard–Marangoni convection. *Appl. Phys. Lett.* **79**, 439–441.

KABOVA, Y. O., ALEXEEV, A., GAMBARYAN-ROISMAN, T. & STEPHAN, P. 2006 Marangoni-induced deformation and rupture of a liquid film on a heated microstructured wall. *Phys. Fluids* **18**, 012104.

KŐRÖSI, G. & KOVÁTS, E. S. 1981 Density and surface tension of 83 organic liquids. *J. Chem. Engng Data* **26**, 323–332.

MILLS, K. C., KEENE, B. J., BROOKS, R. F. & SHIRALI, A. 1998 Marangoni effects in welding. *Phil. Trans. R. Soc. Lond.* A **356**, 911–925.

MÜNCH, A. 2002 The thickness of a Marangoni-driven thin liquid film emerging from a meniscus. *SIAM J. Appl. Math.* **62**, 2045–2063.

NAM, J., SCRIVEN, L. E. & CARVALHO, M. S. 2009 Tracking birth of vortex in flows. *J. Comput. Phys.* **228**, 4549–4567.

ORON, A., DAVIS, S. H. & BANKOFF, S. G. 1997 Long-scale evolution of thin liquid films. *Rev. Mod. Phys.* **69**, 931–980.

PHAM, T., CHENG, X. & KUMAR, S. 2017 Drying of multicomponent thin films on substrates with topography. *J. Polym. Sci.* B*: Polym. Phys.* **55**, 1681–1691.

POLING, B. E., THOMSON, G. H., FRIEND, D. G., ROWLEY, R. L. & WILDING, W. V. 2008 Section 2. Physical and chemical data. In *Perry's Chemical Engineers' Handbook* (ed. J. O. Maloney), 2-1–2-517. McGraw-Hill.

POULIKAKOS, D. & BEJAN, A. 1983 The fluid dynamics of an attic space. *J. Fluid Mech.* **131**, 251–269.

RUSSO, A. J., AKAU, R. L. & JELLISON, J. L. 1990 Thermocapillary flow in pulsed laser beam weld pools. *Welding J.* **69**, 23–29.

SADIQ, I. M. R. 2012 First-order energy-integral model for thin Newtonian liquids falling along sinusoidal furrows. *Phys. Rev.* E **85**, 036309.

SADIQ, I. M. R., GAMBARYAN-ROISMAN, T. & STEPHAN, P. 2012 Falling liquid films on longitudinal grooved geometries: integral boundary layer approach. *Phys. Fluids* **24**, 014104.

SAPRYKIN, S., TREVELYAN, P. M. J., KOOPMANS, R. J. & KALLIADASIS, S. 2007 Free-surface thin-film flows over uniformly heated topography. *Phys. Rev.* E **75**, 026306.

SCHATZ, M. F. & NEITZEL, G. P. 2001 Experiments on thermocapillary instabilities. *Annu. Rev. Fluid Mech.* **33**, 93–127.

SCHWABE, D. & SCHARMANN, A. 1981 Marangoni convection in open boat and crucible. *J. Crystal Growth.* **52**, 435–449.

SCRIVEN, L. E. 1960 Dynamics of a fluid interface. *Chem. Engng Sci.* **12**, 98–108.

SEN, A. K. & DAVIS, S. H. 1982 Steady thermocapillary flows in two-dimensional slots. *J. Fluid Mech.* **121**, 163–186.

SIRIGNANO, W. A. & GLASSMAN, I. 1970 Flame spreading above liquid fuels: surface-tension-driven flows. *Combust. Sci. Technol.* **1**, 307–312.

STRANI, M., PIVA, R. & GRAZIANI, G. 1983 Thermocapillary convection in a rectangular cavity: asymptotic theory and numerical simulation. *J. Fluid Mech.* **130**, 347–376.

TELETZKE, G. F., DAVIS, H. T. & SCRIVEN, L. E. 1988 Wetting hydrodynamics. *Rev. Phys. Appl.* **23**, 989–1007.

TOMITA, H. & ABE, K. 2000 Numerical simulation of pattern formation in the Bénard–Marangoni convection. *Phys. Fluids* **12**, 1389–1400.

https://doi.org/10.1017/jfm.2018.812 Published online by Cambridge University Press

TORRANCE, K. E. 1971 Subsurface flows preceding flame spread over a liquid fuel. *Combust. Sci. Technol.* **3**, 133–143.

VAN DYKE, M. 1964 *Perturbation Methods in Fluid Mechanics*. The Parabolic Press.

WEINSTEIN, S. J. & PALMER, H. J. 1997 Capillary hydrodynamics and interfacial phenomena. In *Liquid Film Coating* (ed. S. F. Kistler & P. M. Schweizer), pp. 19–62. Chapman and Hall.

ZENG, W., SHU, L., LI, Q., CHEN, S., WANG, F. & TAO, X. M. 2014 Fiber-based wearable electronics: a review of materials, fabrication, devices, and applications. *Adv. Mater.* **26**, 5310–5336.

ZIENKIEWICZ, O. C. & TAYLOR, R. L. 2000 *The Finite Element Method*. Butterworth-Heinemann.

https://doi.org/10.1017/jfm.2018.812 Published online by Cambridge University Press